

# Detecting active latitudes of Sun-like stars using asteroseismic a-coefficients

Othman Benomar<sup>123</sup>, Masao Takata<sup>4</sup>, Michael Bazot<sup>5</sup>, Takashi Sekii<sup>12</sup>, Laurent Gizon<sup>367</sup>, and Yuting Lu<sup>8</sup>

<sup>1</sup> Department of Astronomical Science, School of Physical Sciences, SOKENDAI, 2-21-1 Osawa, Mitaka, Tokyo 181-8588 e-mail: othman.benomar@nao.ac.jp, ob19@nyu.edu

<sup>2</sup> Solar Science Observatory, National Astronomical Observatory of Japan, 2-21-1 Osawa, Mitaka, Tokyo 181-8588, Japan

<sup>3</sup> New York University Abu Dhabi, Center for Space Science, PO Box 129188, UAE

<sup>4</sup> Department of Astronomy, School of Science, The University of Tokyo, 7-3-1 Hongo, Bunkyo-ku, Tokyo, 113-0033, Japan

<sup>5</sup> Heidelberg Institut für Theoretische Studien, Schloss-Wolfsbrunnenweg 35, 69118 Heidelberg, Germany

<sup>6</sup> Max-Planck-Institut für Sonnensystemforschung, 37077, Göttingen, Germany

<sup>7</sup> Institut für Astrophysik, Georg-August-Universität Göttingen, 37077, Göttingen, Germany

<sup>8</sup> Department of Physics, The University of Tokyo, Tokyo 113-0033, Japan

Received 30 May 2023 Accepted August 16, 2023

## ABSTRACT

**Aims.** We introduce a framework to measure the asphericity of Sun-like stars using  $a_1$ ,  $a_2$  and  $a_4$  coefficients, and constrain their latitudes of magnetic activity.

**Methods.** Systematic errors on the inferred coefficients are evaluated in function of key physical and seismic parameters (inclination of rotation axis, average rotation, height-to-noise ratio of peaks in power spectrum). The measured a-coefficients account for rotational oblateness and the effect of surface magnetic activity. We use a simple model that assumes a single latitudinal band of activity.

**Results.** Using solar SOHO/VIRGO/SPM data, we demonstrate the capability of the method to detect the mean active latitude and its intensity changes between 1999–2002 (maximum of activity) and 2006–2009 (minimum of activity). We further apply the method to study the solar-analogue stars 16 Cyg A and B using Kepler observations. An equatorial band of activity, exhibiting intensity that could be comparable to that of the Sun, is detected in 16 Cyg A. However, 16 Cyg B exhibits a bi-modality in  $a_4$  that is challenging to explain. We suggest that this could be a manifestation of the transition between a quiet and an active phase of activity. Validating or invalidating this hypothesis may require new observations.

**Key words.** stars:activity, stars:rotation, stars:solar-type, asteroseismology

## 1. Introduction

The observations from the space-borne instruments MOST (Walker et al. 2003), CoRoT (Baglin et al. 2006), *Kepler* (Borucki et al. 2010) and TESS (Ricker et al. 2014) have been important in advancing our knowledge of stellar interiors. This is particularly true for *Kepler*, which could observe continuously tens of thousand of stars for nearly four continuous years, enabling asteroseismic measurements that almost rival disk-integrated helioseismic measurements from a decade ago. Those precise measurements have for example enabled us to better understand stellar rotation and its impact on stellar evolution. The asteroseismology of Sun-like stars is based on the study of the pressure modes that are excited by turbulent convection in the outer layers of these stars. The acoustic modes may reach deep into the core or may be localised close to the stellar surface, giving access to the internal structure and dynamics of the stars. Rotation has a critical impact on the stellar structure and evolution as it induces a material mixing process (Maeder & Meynet 2008). Rotation is also an essential ingredient of the dynamo-effect (Thompson et al. 2003) and can lead to a distortion of the star’s shape due to the centrifugal force (Chandrasekhar 1969). For fast rotators, the rotational flattening must be taken into account. These stars show a variety of pulsation modes that are not present in slower rotators (e.g. Lignières et al. 2006).

Despite its slow rotation rate, the solar asphericity can be measured by helioseismology. While the Sun is seen as oblate by acoustic modes during the quiet phases of its activity cycle, the modes feel a more complicated shape during activity maxima. During solar maxima, the frequencies of acoustic modes increase slightly due to the presence of active regions. The perturbation occurs near the surface and is stronger for modes that sense the active latitudes (below  $\approx 30^\circ$  for the Sun). Physically the magnetic perturbations consist of several components that are not easy to disentangle (incl. stratification and wave speed perturbations (Libbrecht & Woodard 1990; Antia et al. 2000; Dziembowski et al. 2000)). The magnetic perturbations affect the acoustic modes near the surface over only a few hundred kilometres, that is of order  $10^{-5} R_\odot$ , but is significant enough to be measured.

The origin of stellar activity is not well understood as it depends on the complex interplay between rotation, convection and the magnetic field (Brun & Browning 2017). Stellar magnetic cycles are observed in most cool stars (Simon et al. 2002) over a large range of the electromagnetic spectrum and evidence of activity cycles is observed in X-ray (eg. Catura et al. 1975), radio waves (White 1999; White et al. 2017), chromospheric emission lines (Vaughan 1983; Oláh et al. 2009, 2016), and also through luminosity variation due to surface magnetic activity in the visible (Hartmann & Rosner 1979; Silva-Valio et al. 2010; Ceil-

lier et al. 2017). On Sun-like stars, the level of activity is often observed to be cyclic, with activity periods ranging from a few years to decades. Although there are relationships between the stellar age, the rotation period, and the level of activity (van Saders et al. 2016), the underlying mechanisms at play are not understood.

Since the advent of space-borne photometry and the observation of Sun-like pulsators by CoRoT, it became evident that helioseismic methods used for the Sun may be applied to asteroseismic observations. This has resulted in robust estimates of the average rotational splittings, which, in combination with the surface rotation rates inferred from photometric variability, indicate that main sequence stars have nearly-uniform internal rotation rates, (Gizon et al. 2013; Benomar et al. 2015; Nielsen et al. 2017). All of the recent seismic studies of radial differential rotation agree that angular momentum transport in the radiative zone is much more efficient than considered in theory, even in the case of stars more massive than Sun-like stars, such as  $\gamma$ -Doradus stars (eg. Mosser et al. 2012; Gehan et al. 2018; Ouazzani et al. 2019). For the best Kepler observations, asteroseismology showed evidence of latitudinal differential rotation for main sequence stars (Benomar et al. 2018a) and of the radial differential rotation in RGB (e.g. Deheuvels et al. 2012, 2014).

This paper aims at providing a framework to study stellar activity and its latitude by analysing its effect on pulsation frequencies. The proposed method involves the use of the  $a$ -coefficient decomposition (Schou et al. 1994; Pijpers 1997, 1998) on the stellar power spectrum, conveniently separating the perturbations caused by rotation and asphericity. The method is tested on Sun-as-a-star data and on the solar-analogues 16 Cyg A and B, which are the two brightest stars in the initial Kepler observation field.

Only few successful measurements of the asphericity of other stars than the Sun have been made so far. Using ultra-precise measurements of the frequency splittings of time-harmonic (i.e. non-stochastic) low-degree p-modes, Gizon et al. (2016) inferred the oblateness of the  $\gamma$  Doradus– $\delta$  Scuti star KIC 11145123 to be  $\Delta R = (1.8 \pm 0.6) \times 10^{-6} R \approx 3 \pm 1$  km, i.e. smaller than expected from rotational oblateness alone, suggesting the presence of magnetic activity at low latitudes. Bazot et al. (2019) measured the asphericity of the solar-like pulsators 16 Cyg A and B and found that 16 Cyg A is likely prolate, implying that this star may have low-latitude magnetic activity on its surface.

In the spirit of the study by Gizon (2002), we will perform monte-carlo simulations to demonstrate the possibility of inferring the even- $a$  coefficients from simulated oscillation power spectra to constrain the latitude of activity. Unlike Gizon (2002) who included only the  $a_2$  coefficient in the parametric model, we will infer both the  $a_2$  and  $a_4$  coefficients. We start in Section 2 by introducing the effects of rotation on pulsation frequencies and discuss the effect of the centrifugal force and of the activity on the mode cavities. Section 3 presents the assumptions required for the asteroseismic measurement of stellar activity. Section 4 discusses the achievable accuracy of the seismic observables, while sections 5 and 6 present the results on solar data and for 16 CygA and B. This is followed by a discussion and conclusion in section 7.

## 2. The effect of rotation and of magnetic activity

This section presents the effect of rotation and of magnetic activity on pulsation modes, and introduces the frequency model used for asteroseismic data analysis.

### 2.1. Frequency splittings

Slowly rotating stars without significant magnetic activity are approximately spherical and it is common to describe the family of modes travelling inside it using spherical harmonics (see e.g. Unno et al. 1989). If the departure from spherical shape remains small enough, it is convenient to keep the spherical representation for the equilibrium model and account for distortions through a perturbation analysis. All pulsations can then be described using a set of integers  $(n,l,m)$ , namely the radial order, the mode degree and the azimuthal order, respectively. Acoustic pressure modes observed in Sun-like stars can be identified using their frequencies  $\nu_{nlm}$ .

In a non-rotating, non-active star,  $m$ -components are degenerate and cannot be resolved. When rotation or magnetic activity sets in, this degeneracy is lifted. The resulting frequency is treated as a perturbation to the degenerate frequency without rotation and activity,

$$\nu_{nlm} = \nu_{nl} + \delta\nu_{nlm}, \quad (1)$$

with  $\nu_{nl}$ , the equilibrium eigenfrequency without rotation and activity and  $\delta\nu_{nlm}$  the frequency splitting. These splitting may depend on multiple physical effects perceived by the modes (Libbrecht & Woodard 1990) within their cavity of propagation. These can be terms of order  $O(\Omega)$ , with  $\Omega$  the rotation rate estimated at the equator,  $\Omega = \Omega(r, \theta = \pi/2)$ . These depend directly on the stellar rotation profile  $\Omega(r, \theta)$ . Higher-order perturbations pertaining to the shape of the mode cavity can also exist. Note that  $\nu_{nl}$  differs from  $\nu_{nl,m=0}$  as the  $m = 0$  components may have their frequency shifted by perturbations such as the magnetic activity (see e.g. Figure 1).

Splitting can be described using the Clebsch-Gordan  $a$ -coefficient decomposition (Ritzwoller & Lavelle 1991), that corresponds to a representation of the splittings on a basis of polynomials  $\mathcal{P}_j^{(l)}(m)$  of degree  $j$  in  $m$ ,

$$\delta\nu_{nlm} = \sum_{j=1}^{j_{max}} a_j(n, l) \mathcal{P}_j^{(l)}(m), \quad (2)$$

with the polynomials such that

$$\sum_{m=-l}^l \mathcal{P}_i^{(l)}(m) \mathcal{P}_j^{(l)}(m) = 0 \text{ when } i \neq j. \quad (3)$$

Here,  $a_j(n, l)$  is the  $a$ -coefficient of order  $j$  and  $j_{max} = 2l$  is the maximum order to which the decomposition must be carried for a given degree. The standard set of polynomials used in this expansion are those normalised as per described by Schou et al. (1994).

This decomposition is extensively used in helioseismology and was used on Sun-like stars by Benomar et al. (2018a). Asteroseismology has been so far unable to observe modes of degree higher than  $l = 3$  so that in the following the discussion is restricted to  $l \leq 3$  and  $j_{max} = 2l = 6$ , due to the selection rule of the  $\mathcal{P}_j^{(l)}(m)$ . This limitation is the consequence of full-disk integrated photometric observations. An example of splitting including odd and even  $a_j$  coefficients is given in Figure 1 for  $l = 1, 2$ .

This theoretical model leads to a natural interpretation of the observed splittings. One may decomposes these latter into their symmetrical,  $S_{nlm}$ , and anti-symmetrical,  $T_{nlm}$ , parts. These components can then be described as sums over, respectively, the odd

161 and even a-coefficients,

$$S_{nlm} = \frac{\nu_{n,l,m} - \nu_{n,l,-m}}{2m} = \frac{1}{m} \sum_{j=1}^{j_{\max}/2} a_{2j-1}(n, l) \mathcal{P}_{2j-1}^{(l)}(m), \quad (4)$$

$$T_{nlm} = \frac{\nu_{n,l,m} + \nu_{n,l,-m}}{2} - \nu_{n,l,0} = \sum_{j=1}^{j_{\max}/2} a_{2j}(n, l) (\mathcal{P}_{2j}^{(l)}(m) - \mathcal{P}_{2j}^{(l)}(0)). \quad (5)$$

162 This arises from the parity relation  $\mathcal{P}_j^{(l)}(-m) = (-1)^j \mathcal{P}_j^{(l)}(m)$ .  
163 These equations can be used to express the a-coefficients with  
164  $S_{nlm}$  and  $T_{nlm}$ . They also provide relations between the  $\nu_{nlm}$  with  
165 the  $a_j(n, l)$  (Appendix A.2).

166 It can be seen from Appendix A.1 that the sums in Eqs. (4)  
167 and (5) involve, respectively, odd and even functions of  $m$ . Phys-  
168 ically, this means that the symmetrical components of the split-  
169 tings (Gough & Thompson 1990) result from large-scale per-  
170 turbations sensitive to the prograde or retrograde nature of the  
171 waves, such as advection or the Coriolis force. On the other  
172 hand, the anti-symmetric splittings are caused by processes that  
173 are not affected by the propagation direction of waves. This may  
174 include the centrifugal force, that scales as  $O(\Omega^2)$ , and whose ef-  
175 fect on the oscillation frequencies varies as  $m^2$ . Magnetic fields  
176 or non-spherical deformations of the equilibrium structure will  
177 also contribute to the anti-symmetric splittings.

178 We further decompose the anti-symmetric splittings into a  
179 term depending on centrifugal-force-induced distortions and an-  
180 other one accounting for activity-related distortions,

$$T_{nlm} = \delta\nu_{nlm}^{(CF)} + \delta\nu_{nlm}^{(AR)}. \quad (6)$$

181 The symmetric part of the splitting corresponds to a term  $\delta\nu_{nlm}^{(rot)}$   
182 that stems from perturbations of order  $O(\Omega)$  and the total ob-  
183 served splitting is,

$$\delta\nu_{nlm} = \delta\nu_{nlm}^{(rot)} + \delta\nu_{nlm}^{(CF)} + \delta\nu_{nlm}^{(AR)}. \quad (7)$$

184 Using the Sun as an archetype of Sun-like star, it is possible to  
185 measure these contributions to  $\delta\nu_{nlm}$  as shown in Sections 2.2  
186 and 2.3.

## 187 2.2. Expressions for $\delta\nu_{nlm}^{(rot)}$ , $\delta\nu_{nlm}^{(CF)}$ and $\delta\nu_{nlm}^{(AR)}$

188 To the first order, the perturbation on the frequency due to rota-  
189 tion is,

$$\delta\nu_{nlm}^{(rot)} = \frac{m}{2\pi} \int_0^R \int_0^\pi K_{nlm}(r, \theta) \Omega(r, \theta) r dr d\theta, \quad (8)$$

190 where  $R$  is the radius of the star and the kernel  $K_{nlm}(r, \theta)$  (Hansen  
191 et al. 1977) expresses the sensitivity of a mode to the rotation at  
192 the radial point  $r$  and co-latitude  $\theta$ .  $\Omega(r, \theta)$  is the rotation profile  
193 of the star. It can be shown that  $\delta\nu_{nlm}^{(rot)}$  actually only depends  
194 on symmetrical splittings (Ritzwoller & Lavelle 1991) which in  
195 turns depend only on odd coefficients. For example and for  $l = 3$ ,  
196 it is expressed as,

$$\delta\nu_{nlm}^{(rot)} \simeq \mathcal{P}_1^{(l)}(m) a_1 + \mathcal{P}_3^{(l)}(m) a_3 + \mathcal{P}_5^{(l)}(m) a_5. \quad (9)$$

197 Centrifugal forces typically distorts a spherical rotating  
198 sphere of gas into an oblate ellipsoid, elongated at the equa-  
199 tor. Functional analysis shows that the contribution of centrifugal  
200 forces to the mode splitting scales with  $\Omega^2 R^3 / GM$ . Properly inte-  
201 grating higher-order terms of the perturbation expansion over the

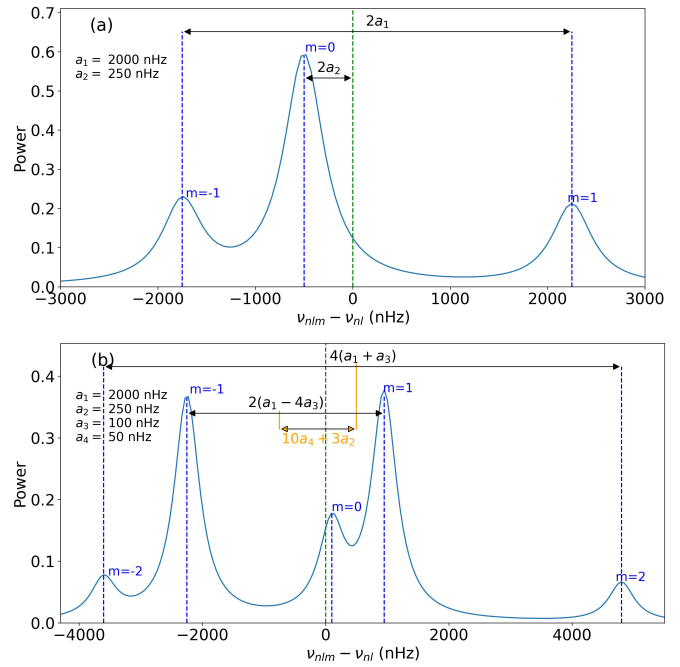


Fig. 1. Example of Lorentzian mode profiles showing the a-coefficients and their relationship with frequency spacings for  $l = 1$  (a) and  $l = 2$  modes (b). The orange spacing is  $T_{n22} - T_{n21}$ .  $\nu_{nl}$  is the m-averaged frequency of each multiplet. The stellar inclination is  $40^\circ$ .

202 aspherical volume of the star and using asymptotic expressions 203 for the equilibrium mode eigenfunctions (assuming  $n$  is large 204 enough), leads to the following expression for the centrifugal- 205 force component of the frequency splitting (Gough & Taylor 206 1984; Gough & Thompson 1990),

$$\delta\nu_{nlm}^{(CF)} = \frac{\Omega^2 R^3}{GM} \nu_{nl} Q_{lm}, \quad (10)$$

207 with  $Q_{lm} \approx \frac{2}{3} \frac{l(l+1)-3m^2}{(2l-1)(2l+3)}$  factor depending on the density. Equation 208 (10) means that

$$\delta\nu_{nlm}^{(CF)} = \mathcal{P}_2^{(l)}(m) a_2^{(CF)}(n, l) \quad (11)$$

with

$$a_2^{(CF)}(n, l) = -\frac{1}{2l+3} \frac{\Omega^2 R^3}{GM} \nu_{nl} \quad (12)$$

210 since  $-(2l+3)Q_{lm} = \mathcal{P}_2^{(l)}(m)$ . It should be noted that the con- 211 tribution of the centrifugal-force-induced deformation to the fre- 212 quency splittings can be described by a linear combination of 213 the  $\mathcal{P}_{2j}$  polynomials (Gough & Taylor 1984; Gough & Thomp- 214 son 1990). Since the stars are assumed to be slowly rotating, one 215 may only retain terms of order  $O(\Omega^2)$ , which correspond to the 216 contribution of the  $a_2$  coefficient alone.

217 One can further approximate equation (12) in order to ex- 218 press  $\delta\nu_{nlm}^{(CF)}$  as a function of quantities that can be obtained di- 219 rectly from the modelling of the acoustic power spectra of Sun- 220 like stars (Benomar et al. 2018a). First, the stellar mean den- 221 sity of a Sun-like star scales to a good approximation with its 222 large separation, that is the average distance in the frequency 223 space between modes of identical degree and consecutive or- 224 ders (Ulrich 1986). In solar units, this reads  $\rho = (\rho_\odot / \Delta\nu_\odot) \Delta\nu$ , 225 with the solar density  $\rho_\odot = (1.4060 \pm 0.0005) \times 10^3$  kg m<sup>-3</sup> and 226

*226*  $\Delta\nu_{\odot} = 135.20 \pm 0.25 \mu\text{Hz}$  (García et al. 2011b). With an accuracy estimated to a few percents for Sun-like stars (White et al. 2011), the use of this scaling relation is thought to be a decent approximation.

*230* The second simplification uses the fact that the Clebsch-Gordan coefficient decomposition of the frequency splitting imposes a one-to-one relationship between the a-coefficients and the coefficients of the decomposition of the velocity field into poloidal and toroidal components (Ritzwoller & Lavelle 1991). Helioseismology suggests that the Sun rotates with a near constant angular velocity down to at least  $r/R_{\odot} = 0.2$  (e.g. Thompson et al. 2003), which is the maximum depth at which measurements from low-degree p modes are available. Furthermore, its outer-convective zone shows a differential rotation of  $\simeq 30\%$  from the equator to the pole, which leads to an  $a_{3,\odot}(n, l) \simeq 4 \text{ nHz}$  and to even smaller values for higher odds a-coefficients. This is significantly smaller than  $a_{1,\odot}(n, l) \simeq 420 \text{ nHz}$ . Therefore, the aforementioned one-to-one relation ensures that we can retain only the leading order in the expansion of the rotation rate and treat it as an average value, given in terms of seismic observables by  $\Omega \simeq 2\pi a_1$ . This leads to

$$a_2^{(CF)}(n, l) \simeq -\frac{\nu_{nl}}{2l+3} \frac{3\pi}{G\rho_{\odot}} \frac{\Delta\nu_{\odot}^2}{\Delta\nu^2} a_1^2. \quad (13)$$

*247* Regarding  $\delta\nu_{nlm}^{(AR)}$ , there is no unambiguous theory to describe *248* the effect of the near-surface magnetic activity on the shape of *249* the cavity. Due to this and following Gizon (2002), a geometrical *250* description is preferred to a physical model. This description assumes that the corresponding wave-speed perturbation separates *251* in the latitudinal and radial coordinates. The proposed form of *252* the perturbation in frequency is,

$$\begin{aligned} \delta\nu_{nlm}^{(AR)} &= \nu_{nl}\epsilon_{nl} \int_0^{2\pi} \int_0^{\pi} F(\theta|\mathbf{x}) |Y_l^m(\theta, \phi)|^2 \sin\theta d\theta d\phi \\ &= \nu_{nl}\epsilon_{nl} A_{lm}(\mathbf{x}) \\ &= \sum_{j=0}^{j_{\max}/2} \mathcal{P}_{2j}^{(l)}(m) a_{2j}^{(AR)}(n, l). \end{aligned} \quad (14)$$

*255* The term  $a_{2j}^{(AR)}(n, l)$  in equation (14) refers to the combined contribution of a magnetic field and other perturbations in the stellar structure (e.g. stratification, temperature). The geometrical weight function  $A_{lm}(\mathbf{x})$  describes the effect of an active zone at the co-latitude  $\theta$ , on a mode of degree  $l$  and azimuthal order  $m$ . *256*  $A_{lm}(\mathbf{x})$  is the product of two contributions. First, the normalised *257* spherical harmonics  $Y_l^m(\theta, \phi)$  that decompose the magnetic activity effect over each modes. These are spherical-polar coordinates defined in the inertial frame with a polar axis pointing in *258* the direction of the rotation axis. Second, the weight distribution *259* (or the shape of the active region) is defined by  $F(\theta|\mathbf{x})$ . Here,  $\mathbf{x}$  *260* refers to the parameters that are necessary to describe the function *261*  $F(\theta|\mathbf{x})$ .

*262* On the Sun, large active regions persist on the surface for 1-2 *263* rotation periods and are randomly distributed in longitude over *264* well defined latitudes. Here we assume that the corresponding *265* perturbation can be approximated by a function of latitude only. *266* The general problem of distinct active regions on the differentially rotating surface would go beyond the present study (see *267* Papini & Gizon 2019, for the case of a single long-lived active *268* region). In this paper, we only consider perturbations that are approximately steady in the inertial frame (i.e. latitudinal bands of *269* activity).

*270* In theory, a third integral over the radius is necessary to *271* describe the dependence of the magnetic activity to the stellar *272* depth. However, p modes are weakly sensitive to the deep structure *273* inside stars. Here, the radial integral is replaced by  $\epsilon_{nl}$ , the *274* overall activity intensity. The frequency  $\nu_{nl}$  allows a dimensionless *275*  $\epsilon_{nl}$ , that can be compared between stars. Section 3.2 further *276* develops the required assumptions in order to obtain a reliable *277* information content on the active region in asteroseismology. *278*

### 286 2.3. Modelling the frequencies

Combining equation (1), (7), (8), (13) and (14) leads to,

$$\begin{aligned} \nu_{nlm} &= \nu_{nl} \left( 1 + \frac{3\pi}{(2l+3)G\rho_{\odot}} \frac{\Delta\nu_{\odot}^2}{\Delta\nu^2} a_1^2 \right) \\ &\quad + \epsilon_{nl} A_{lm}(\mathbf{x}) + \frac{m}{2\pi} \int_0^R \int_0^{\pi} K_{nlm}(r, \theta) \Omega(r, \theta) r dr d\theta. \end{aligned} \quad (15)$$

Using equation (1) and (2),  $\nu_{nlm}$  can also be expressed using *287* the a-coefficients without loss of generality,

$$\nu_{nlm} = \nu_{nl} + \sum_{j=1}^{2l} \mathcal{P}_{2j}^{(l)}(m) a_j(n, l). \quad (16)$$

It is possible to use equation (15) in order to measure the activity parameters  $\mathbf{x}$ , by directly fitting the power spectrum. However, there are multiple benefits to use instead a two-step approach consisting in first using equation (16) for the fitting of the power spectrum to evaluate the a-coefficients (method detailed in Appendix B). And then, fitting the coefficients obtained during the first step, using solely the equations (13) and (14) (detailed in Appendix C). Firstly and in the general case, the evaluation of  $A_{lm}(\mathbf{x})$  requires the precise computation of a double integral. This is a slow process, that increases the time necessary to fit the power spectrum<sup>1</sup>. Postponing to an ulterior step the computation of  $A_{lm}(\mathbf{x})$  reduces drastically the parameter space from a few tens of parameters to only a few<sup>2</sup>, effectively making faster the convergence rate of the fitting algorithm and making it easier to explore the assumptions that have to be made on equation (15) in order to have a functional approach in real cases (see the discussions in Section 3). Secondly, it allows us to decouple the observables from the physics, enabling to test various physical assumptions without having to re-perform the lengthy power spectrum analysis. Finally, it eases the evaluation of the reliability of the activity determination, by enabling us to pinpoint the cause of biases (if any) on either the observables (eg.  $a_2$ ,  $a_4$ , see Section 4) or on the interpretation of these observables in terms of physical parameters (see Section 3.3). The disadvantage of the two-step approach is that it requires more statistical assumptions, such as neglecting correlations and assuming Gaussian parameters. Although one can argue that it is possible to perform a hierarchical Bayesian analysis (eg. Hogg et al. 2010; Campante et al. 2016) to partly alleviate this issue, such an approach is generally slow and may cancel the benefits of the two-step approach.

### 320 3. Information content in low order a-coefficients

The general theoretical formulations of Section 2, demonstrate *321* how pulsation frequencies are expressed as function of the rota- *322*

<sup>1</sup>Using a MCMC method, from a day to a couple of weeks for a single star on a present-day CPU

<sup>2</sup>With our choice of  $A_{lm}(\mathbf{x})$ , three parameters are fitted. See section 3.2.

323 tion, the centrifugal distortion and the activity of stars. However,  
 324 observational limitations need to be accounted to enable a vi-  
 325 able, robust model that extract as much possible the information  
 326 content within currently existing data. This necessarily requires  
 327 additional assumptions, for which the rational is detailed here-  
 328 after.

### 329 3.1. Factors contributing to the splitting accuracy and 330 precision

331 As explained in Kamiaka et al. (2018), the pulsation height ( $H$ )  
 332 and the noise background ( $N$ ) are important factors that reduce  
 333 the capabilities of asteroseismic analyses. Those are a complex  
 334 function of the global stellar characteristics (mass, radius, age),  
 335 of the convective motion at the surface of Sun-like stars, and also  
 336 depend on the instrumental limitations. The mode height and the  
 337 noise background are in fact difficult to evaluate *a priori*. How-  
 338 ever, the Height-to-Noise (HNR), defined as the ratio  $H/N$  can  
 339 be used to assess the quality of the spectrum of a pulsation mode.  
 340 In fact, Kamiaka et al. (2018) show that the HNR at maximum of  
 341 mode height  $\widehat{HNR}$ , can be used to study biases on the stellar in-  
 342 clination. This is because all main sequence Sun-like stars show  
 343 a similar dependency of the height and of the width as a function  
 344 of the frequency (see e.g. Appourchaux et al. 2014). In Section  
 345 4, we propose the same, but on a-coefficients.

346 The  $\widehat{HNR}$  not only defines how many modes can be ob-  
 347 served, but also the maximum degree of the modes that is ob-  
 348 served. Considering specifically the Kepler observations, stars  
 349 exhibit a  $\widehat{HNR}$  for  $l = 0$  modes of up to 30, the highest HNR  
 350 being observed for 16 Cyg A and 16 Cyg B. Kamiaka et al.  
 351 (2018) showed that the capability of distinguishing rotationally  
 352 split components is of great importance if one wants to obtain  
 353 a reliable asteroseismic inference of the rotation characteristics  
 354 and of the stellar inclination. In particular, the ratio  $a_1/\Gamma_{v_{max}}$  be-  
 355 between the  $a_1$  coefficient and the mode width determined at the  
 356 maximum of mode amplitude  $\Gamma_{v_{max}}$  (see Figure 6), determines  
 357 the expected bias on the stellar inclination. As shown in Sec-  
 358 tion 4,  $a_1/\Gamma_{v_{max}}$  also controls the importance of the bias for the  
 359 other low order a-coefficients. Finally, another important factor  
 360 is the spectrum resolution. The higher the resolution, the more  
 361 resolved are the modes. Thus, observations  $T_{obs}$  of several years  
 362 are the most suitable in order to resolve and measure rotation-  
 363 ally split components. Broadly speaking, observations exceeding  
 364 a year and  $a_1/\Gamma > 0.4$  are preferable to ensure a reliable  
 365 measurement of  $a_1$ .

366 All of the limitations discussed above incite us to introduce  
 367 assumptions to ensure robust measurements of a-coefficients (ie,  
 368 mitigate biases).

### 369 3.2. Latitudinal profile of the activity

370 Noting that it is challenging to measure low-degree a-coefficients  
 371 for the Sun (eg. Toutain & Kosovichev 2001), we present here a  
 372 minimal set of assumptions on even a-coefficients allowing us  
 373 to constrain the asphericity of stellar cavities. One of the first  
 374 aspects that has to be considered is the form of  $F(\theta|x)$ , the function  
 375 characterising the activity latitude  $\theta$  (see equation (14)).

376 The butterfly diagram of the Sun (Figure 2) is used as a ref-  
 377 erence for this latitudinal dependence. The data are from the  
 378 Greenwich USAF/NOAA observatory<sup>3</sup> and provide the daily  
 379 area of the spots, counted manually over the period 1874–2016.  
 380 The panel (a) on Figure 2 shows the butterfly diagram with

381 colours representing the area covered by the spots in unit of per-  
 382 cent of visible hemisphere. It focuses on the observations after  
 383 1985 and covers two full solar cycles. Vertical colour bands high-  
 384 light three time intervals : 1985–1989 (Purple), 1999–2002 (Blue)  
 385 and 2006–2009 (Yellow). The two first are during a maximum of  
 386 solar activity while the last one is for a minimum of activity. Due  
 387 to the gradual migration of the spots over time, the longer ob-  
 388 servation period (1985–1989, 4 years) leads to a broader activity  
 389 zone than the period 1999–2002. This indicates that the extension  
 390 of the active region may not be trivial to measure in other stars  
 391 because it will depend on the fraction of time the star is observed  
 392 relative to the duration of its activity cycle. The activity cycles  
 393 of Sun-like stars (if any) is *a priori* unknown, but Ca II H+K line  
 394 emission and photometric studies (Oláh et al. 2009, 2016) sug-  
 395 gest that it is of durations of roughly a few years to decades, as  
 396 for the Sun. It indicates that over the course of several years, an  
 397 active band as large as  $\approx 40^\circ$  may be expected.

398 Panel (b) of Figure 2 shows the cumulative area of spots as a  
 399 function of the latitude and for the three considered periods. As  
 400 noted earlier, the extension of the activity band is larger for the  
 401 longest time-frame. The area of the spots during the active solar  
 402 phase are symmetrical towards the equator. This suggests that  
 403 when the activity is strong,  $F(\theta|x)$  is almost north-south sym-  
 404 metric. This may be inaccurate for low activity phase, as shown  
 405 for the period 2006–2009 but because  $|Y_l^m(\theta, \phi)|^2$  is also symmet-  
 406 rical towards the equator, this has no incidence on the  $a_j^{(AR)}(n, l)$   
 407 coefficients.

408 During the minimum, the total average area of the spots is  
 409 a few times lower than during the maximum. It is also nar-  
 410 rower, such as the integral in equation (14) is small, reducing  
 411  $a_j^{(AR)}(n, l) \approx 0$ . During the phase of minimum of activity, the ac-  
 412 tivity can effectively be considered as nonexistent (see Section  
 413 5 for the analysis on solar data), so that  $a_2(n, l)$  is dominated by  
 414 the centrifugal term  $a_2^{(CF)}(n, l)$  and the other even a-coefficients  
 415 are null.

416 The overall latitudinal profile is seemingly following a bell-  
 417 shape with sharp slopes during periods of activity. Figure 2c  
 418 compares data between 1986 and 2016 with three models for  
 419 the active latitudes: a model using the gate function  $F(\theta|x) =$   
 420  $\Pi(\theta_0, \delta)$ , a triangular function  $\Lambda(\theta_0, \delta)$  and a Gaussian function  
 421  $\mathcal{N}(\theta_0, \delta)$ . The parameters of these were adjusted manually to ap-  
 422 proximately match the solar spot active latitudes profile. The  
 423 triangular and the Gaussian functions describe equivalently the  
 424 data, while the gate function initially proposed by Gizon (2002)  
 425 is roughly fitting the data. Because spots are strictly appearing  
 426 at latitudes below  $45^\circ$ , the  $\Lambda$  function may be the most suitable  
 427 for the Sun. Nevertheless, these three functions are retained and  
 428 compared here-further.

### 429 3.3. Assumptions on the a-coefficients

430 The most direct method for measuring the asphericity is to eval-  
 431 uate it directly for each mode  $(n, l)$ , that is, measuring the terms  
 432  $a_j(n, l)$ . This being already difficult for low-order a-coefficients  
 433 of the Sun (Chaplin et al. 2003), it seems unreasonable to ex-  
 434 pect an accurate measurement of all individual  $a_j(n, l)$  using as-  
 435 teroseismic data. These have a lower signal-to-noise ratio and  
 436 severely reduced visibility at  $l \geq 3$  due to the integrated photom-  
 437 etry. After a trial and error process, jointly with power spectra  
 438 simulations, we could identify a set of assumptions ensuring re-  
 439 liable and precise measurement of a-coefficients.

440 We first consider a fictitious star rotating as a solid-body  
 441 with a solar activity level ( $\epsilon_{nl} \approx 5 \times 10^{-4}$ , Gizon (2002)) with

<sup>3</sup><https://solarscience.msfc.nasa.gov/greenwch.shtml>

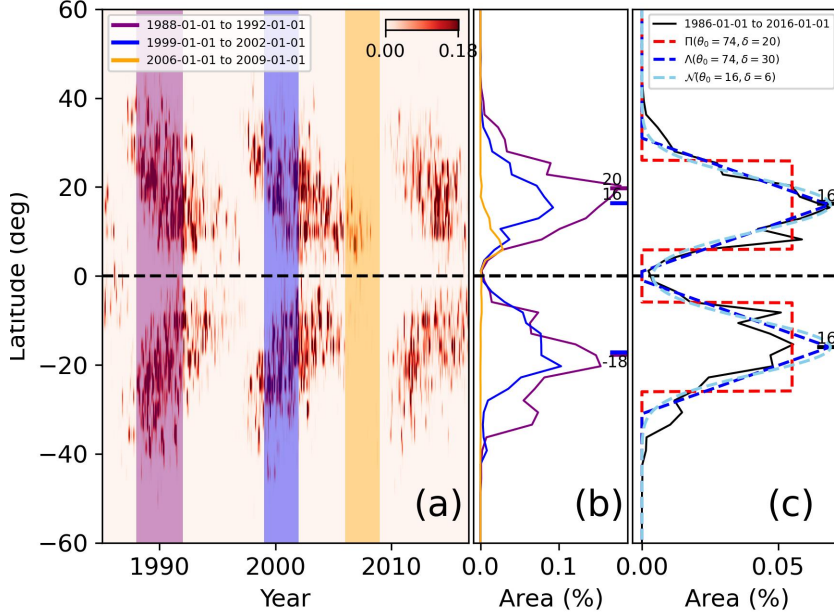


**Fig. 2.** Solar activity over time. (a) Butterfly diagram for the Sun. Vertical colour bands highlight periods of maximum of 1988-1992, 1999-2002 and minimum of activity of 2006-2009. (b) averaged spot area for the highlighted periods. Coloured ticks on (b) are the weighted mean for the activity latitude. (c) Filters  $F(\theta|\theta_0, \delta)$  used for this study superimposed to solar data (1986-2016). Parameters  $\theta_0$  and  $\delta$  are the latitude and the extension of the active region, respectively.

442  $a_1 = 1000$  nHz. The observed oscillation frequencies of 16 Cyg  
 443 A are used here (Davies et al. 2015; Kamiaka et al. 2018). Split  
 444 frequencies are derived using equations (1), (7), (13), (14), and  
 445 converted into a-coefficients using equations (A.8-A.19). The a-  
 446 coefficients are linear functions of the frequency, which is ex-  
 447 pected as  $F(\theta|\theta_0, \delta)$  describes a single active region. Thus, a  
 448 reasonable assumption is to consider those as pure first order  
 449 polynomial functions of frequencies. However, tests on artificial  
 450 spectra showed that it is often difficult to evaluate the slope of  
 451 the a-coefficients. This is because the uncertainty on any  $a_j$  is at  
 452 least of the same order as its variations within the range of ob-  
 453 served frequencies. This suggests that current asteroseismic data  
 454 lack the resolution and the signal-to-noise to reliably measure  
 455 the frequency dependence on the a-coefficients.

456 Figure 3 shows  $a_2^{(AR)}$ ,  $a_4^{(AR)}$ ,  $a_6^{(AR)}$  for activity described by  
 457  $F = \Pi$  (black) or  $\Lambda$  (red) or  $\mathcal{N}$  (blue). These are the mean coeffi-  
 458 cients for the fictitious active star, as a function of  $\theta_0$  and  $\delta$ . The  
 459 figure indicates that there is a simple relationship between the  
 460 a-coefficients, the co-latitude  $\theta_0$  and the extension of the activ-  
 461 ity zone  $\delta$ , independently of the shape of activity. In the case of  
 462  $F = \Pi$ , the lines are cut near the pole and the equator due to the  
 463 condition  $\theta_0 \geq \delta/2$  and  $\theta_0 \leq \pi - \delta/2$ . In the other profiles, edges  
 464 effects (truncation) has noticeable effects near the equator. The  
 465 definition of  $\delta$  differs between the three profiles, which explains  
 466 that a factor of a few in  $a_j^{(AR)}$  is noticeable between  $F = \Pi$ ,  $\Lambda$   
 467 and  $\mathcal{N}$  for a given  $\delta$ . Note that adding the centrifugal effect re-  
 468 duces  $a_2(n, l) = a_2^{(AR)}(n, l) + a_2^{(CF)}(n, l)$ , because the coefficient  
 469  $a_2^{(CF)}(n, l)$  is always negative.

470 If an observation can constrain only a single a-coefficient  
 471 (e.g.  $a_2$ ), there often exists a degeneracy in  $\theta_0$  as multiple value  
 472 of  $a_j$  can be obtained for a given  $\theta_0$ . As the figure shows, mea-  
 473 suring two a-coefficients alleviates this degeneracy, provided that

474 uncertainties are small enough. In other words, the accuracy on  
 475 the inference of the active region using a-coefficients is ensured  
 476 only if we can simultaneously constrain two a-coefficients (e.g.  
 477  $a_2$  and  $a_4$ ). This is essential to distinguish an activity near the  
 478 pole ( $\theta_0 \lesssim 30^\circ$ ) from mid-latitude ( $30^\circ \lesssim \theta_0 \lesssim 60^\circ$ ) or from near  
 479 the equator ( $\theta_0 \gtrsim 60^\circ$ ).

480 It indicates that the loss of information resulting from the  
 481 averaging does not affect the accuracy<sup>4</sup>. Figure 3 also indicates  
 482 that for a star with an activity intensity and an activity zone of  
 483 extension commensurate with the one of the Sun ( $\epsilon_{nl} \approx 5.10^{-4}$ ,  
 484  $\delta \approx 10^\circ$  when  $F = \Pi$ ), the uncertainty on  $a_2^{(AR)}$  must be approxi-  
 485 mately  $\lesssim 25$  nHz, the one for  $a_4^{(AR)} \lesssim 10$  nHz and  $a_6^{(AR)} \lesssim 1.5$  nHz  
 486 to be able to detect significant departures of the coefficients. This  
 487 is to be compared with the spectral resolution of 7-14 nHz for 2-4  
 488 years of observation, typical of the longest Kepler observations.  
 489 In the Figure 3,  $a_2^{(AR)}$  is obtained by averaging  $l = 1, 2$ ,  $a_4^{(AR)}$  by  
 490 averaging  $l = 2$ , while  $a_6^{(AR)}$  is only constrained by  $l = 3$  modes.  
 491 Averaging  $a_2^{(AR)}$  and  $a_4^{(AR)}$  over  $l = 1, 2, 3$  increases the maxi-  
 492 mum range of the a-coefficients by a factor  $\approx 1.5$  for  $a_2^{(AR)}$  and  
 493  $\approx 2$  for  $a_4^{(AR)}$ , respectively, without changing the overall shape  
 494 of the function. In Sun-like stars, the  $l = 3$  modes have a HNR  
 495 at least ten times lower than  $l = 0$  modes because the height ra-  
 496 tio between  $l = 3$  and  $l = 0$  modes is around 0.08 for the Sun  
 497 (Toutain & Gouttebroze 1993; Toutain et al. 1998). These modes  
 498 are therefore difficult to observe. Due to all of the above, it is ex-  
 499 tremely challenging to measure  $a_6$  with current existing data. In  
 500 the following, we will thus focus on assessing the reliability  
 501 domains of  $a_2$  and  $a_4$  only.

<sup>4</sup>It does however increase the uncertainty by a factor of a few.

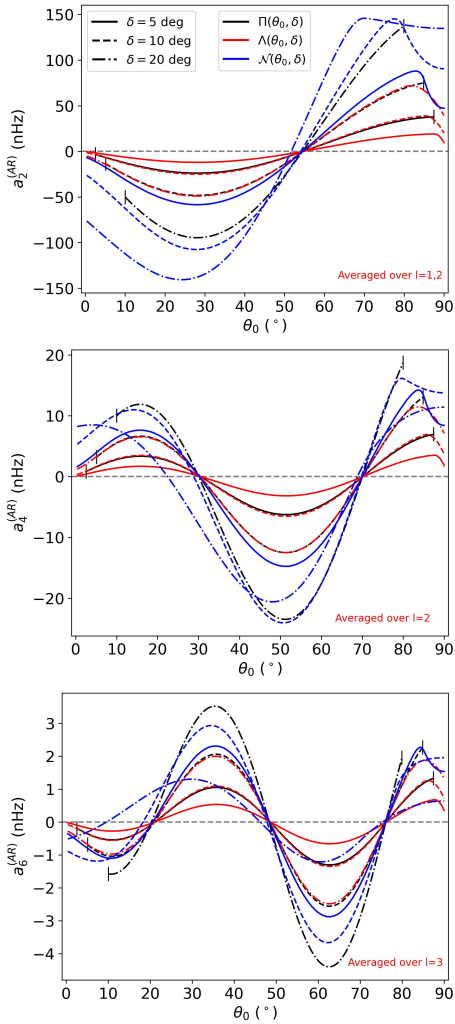


**Fig. 3.** Average  $a_j^{(AR)}$  (no centrifugal effect accounted for) with  $\epsilon_{nl} = 5.10^{-4}$  in function of  $\theta$  and  $\delta$  and for the gate ( $\Pi$ ), triangle ( $\Lambda$ ) and gaussian ( $N$ ) filter functions. Uniqueness is guaranteed for  $\theta$  only if at least two a-coefficients are measured.

#### 4. Bias analysis on $a_1$ , $a_2$ and $a_4$

In order to understand the reliability of the inference on low-degree a-coefficient, it is necessary to perform a bias analysis. This requires to fit an ensemble of emulated spectra that are representative of Sun-like stars and to compare the results with the true inputs.

##### 4.1. Test setup

The synthetic spectra use the frequencies, heights, widths and the noise background profile of 16 Cyg A as a template for the simulations. We want to specifically study the impact of the mode blending (effect of  $a_1/\Gamma_{v_{max}}$ ), the stellar inclination ( $i$ ), observation duration ( $T_{obs}$ ) and of the maximum Height-to-Noise background ( $\widehat{HNR}$ ) on the accuracy of  $a_1$ ,  $a_2$  and  $a_4$ . Grids of spectra are built in the case of an equatorial band of activity and of a large polar activity. The grid parameters and their ranges are provided in Table 4.1 and discussed further below. The spectra are

**Table 1.** Parameters set to construct artificial power spectra.  $a_2$  and  $a_4$  are determined assuming active regions located either in an equatorial band or in a polar cap.

Variable	Values	
HNR	10, 20, 30	
$T_{obs}$ (years)	2, 4	
$a_1/\Gamma_{v_{max}}$	0.4, 0.5, 0.6	
$\epsilon_{nl}$	$5.10^{-4}$	
$a_1$ (nHz)	1000	
Act. Region	$\theta_0 = 85^\circ, \delta = 10^\circ$ (Eq.)	$\theta_0 = 22.5^\circ, \delta = 45^\circ$ (Pol.)
$a_2$ (nHz)	35.41	-205.06
$a_4$ (nHz)	13.52	5.09

made using a spectrum simulator code<sup>5</sup> that take the reference star (or template) and modify its properties to match the requirement of the user. The template is altered in terms of HNR following a similar approach as in Kamiaka et al. (2018). The main difference is that we considered a frequency-dependent noise background. Heights are rescaled according to,

$$H_{n,l=0} = \frac{\widehat{HNR}}{\widehat{HNR}_{ref}} H_{ref}(n, l=0) \quad (17)$$

where  $\widehat{HNR}$  is the maximum HNR of the synthetic star,  $\widehat{HNR}_{ref}$  the maximum HNR of the reference star and  $H_{ref}(n, l=0)$  the  $l=0$  heights of the reference star.

As for the mode blending factor  $f = a_1/\Gamma_{v_{max}}$ , it is calculated fixing  $a_1$  and altering  $\Gamma_{v_{max}}$  such that,

$$\Gamma_{v_{max}} = \frac{a_1}{f}. \quad (18)$$

A fiducial value of  $a_1 = 1000$  nHz ( $\approx 2.4$  the solar rotation) is used in the simulation. Note that this differs from Kamiaka et al. (2018) where the splitting was modified in order to obtain the desired mode blending factor.

As shown in Table 4.1, three HNR cases are investigated, ranging from 10 to 30. Two observation durations are considered: 2 years and 4 years. This is representative of the best Kepler observations (Davies et al. 2015) and of future observations from PLATO (Rauer et al. 2014). Similarly to the test cases of Gizon (2002),  $a_2$  and  $a_4$  are determined for an equatorial activity of extension of the same order as in the Solar case ( $\delta \approx 10^\circ$ ), and in the case of a large polar cap ( $\delta = 45^\circ$ ). Both situations assume an activity of the same order as for the Sun. The priors are set in a similar manner as they would if the power spectrum was from a real star. The evaluation of the mode parameters is performed using a MCMC method, like for actual stars (see Appendix B for further details), but on the limit-spectrum (no noise). Fitting the limit spectrum allows to assess the systematic errors by calculating the expectation value of the probability density function. The expected uncertainty can also be known by computing the standard deviation.

##### 4.2. Results

To appreciate the level of inaccuracy achieved when measuring  $a_j, j \in [1, 2, 4]$  coefficients, the bias is calculated for  $a_j, f =$

<sup>5</sup>The tool suite used here along with the data inputs/outputs are available at [https://github.com/OthmanB/Benomar2022/tree/version\\_2](https://github.com/OthmanB/Benomar2022/tree/version_2).

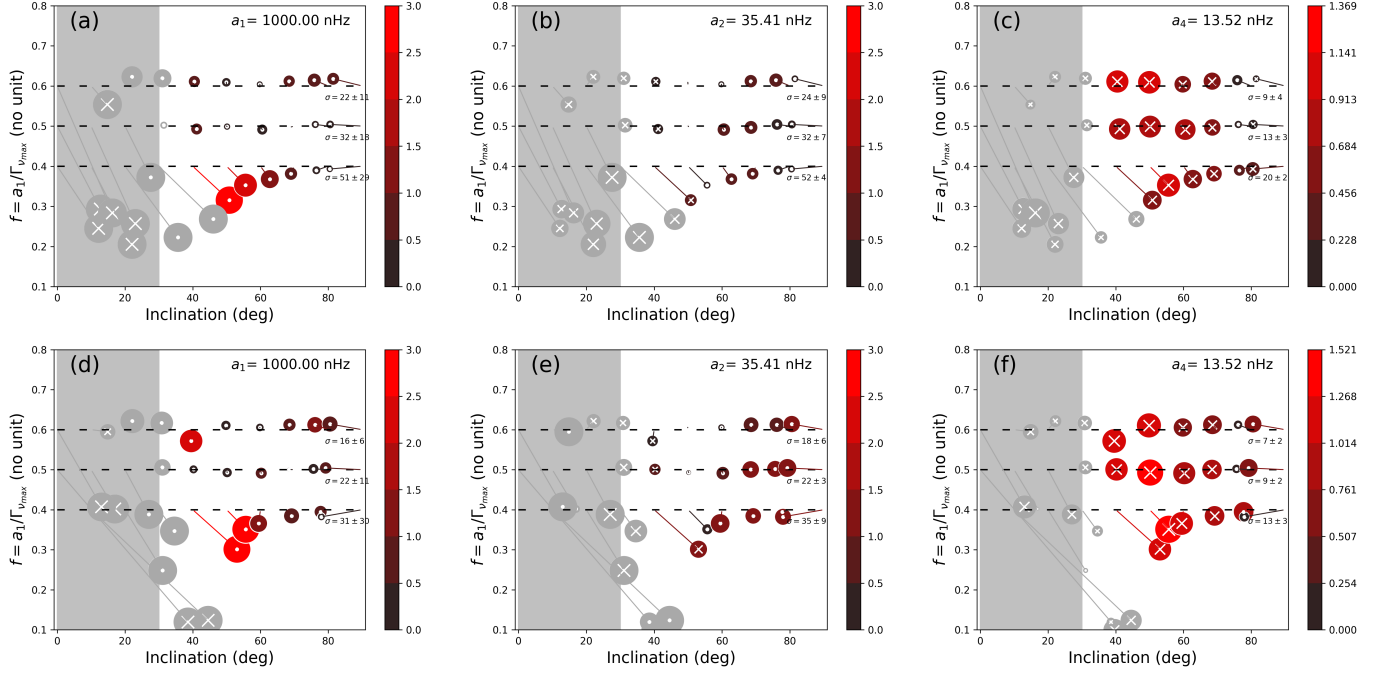


**Fig. 4.** Bias analysis for  $\widehat{HNR} = 30$  for an equatorial activity band ( $\theta_0 = 85^\circ, \delta = 10^\circ$ ) of similar intensity to the Sun ( $\epsilon_{nl} = 5 \times 10^{-4}$ ), for  $T_{obs} = 2$  years (top) and  $T_{obs} = 4$  years (bottom). Colour and size of the circles indicate the modulus of the bias. The colour bar gives its scale normalised by the uncertainty,  $b(a_j)/\sigma$ . A white cross is for an underestimation. A white dot is for an overestimation. Below  $30^\circ$  of inclination (gray area and symbols), the results are not reliable.

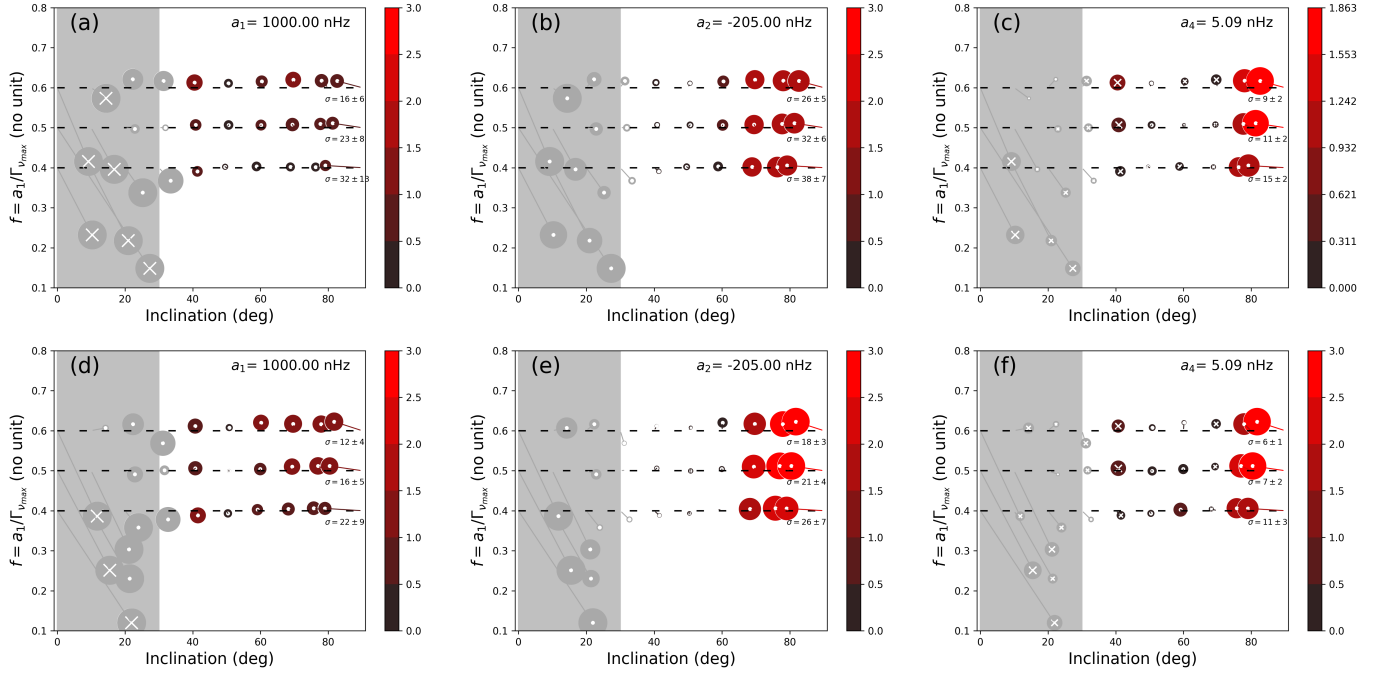


**Fig. 5.** Bias analysis for  $\widehat{HNR} = 30$  for a large polar activity cap ( $\theta_0 = 22.5^\circ, \delta = 45^\circ$ ) of similar intensity to the Sun ( $\epsilon_{nl} = 5.10^{-4}$ ), for  $T_{obs} = 2$  years (top) and  $T_{obs} = 4$  years (bottom).

553  $a_1/\Gamma_{\nu_{max}}$  and  $i$ ,

$$\begin{aligned} b(a_j) &= E[a_j^{\text{meas}}] - a_j^{\text{true}}, \\ b(F) &= E[F^{\text{meas}}] - F^{\text{true}}, \\ b(i) &= E[i^{\text{meas}}] - i^{\text{true}}. \end{aligned} \quad (19)$$

554 Here, the letter E refers to the expectation value (median)  
555 from the probability density function.

556 Figure 4 shows the resulting bias maps for a-coefficients as  
557 a function of the blending factor  $F$  and of the stellar inclination  
558 for a-coefficients corresponding to an equatorial activity band.  
559 Figure 5 is the same but for a large polar activity cap. The bias

**Table 2.** Summary of the main parameters for the Sun and 16 Cyg A and B used to infer the activity. fiducial biases  $b(a_2)$  and  $b(a_4)$  for 16 Cyg A and B are set after inspection of Figure 4. The lowest (highest) solution of  $a_4$  for 16 Cyg B is has a probability of 30% (70%).

	Active Sun	Quiet Sun	16 Cyg A	16 Cyg B
$\widehat{HNR}$	100	70	30	29
$\Delta\nu$ ( $\mu\text{Hz}$ )	135.1	135.1	103.35	116.92
$a_1$ (nHz)	$421 \pm 10$	$410 \pm 9$	$614 \pm 37$	$607 \pm 78$
$a_1/\Gamma$	$0.45 \pm 0.03$	$0.40 \pm 0.02$	$0.45 \pm 0.04$	$0.58 \pm 0.1$
inclination ( $^\circ$ )	90 (fixed)	90 (fixed)	$45 \pm 4$	$35 \pm 3$
$a_2$ (nHz)	$80 \pm 19$	$11 \pm 21$	$19.6 \pm 8.6$	$18.5 \pm 23.5$
$a_4$ (nHz)	$5.0 \pm 10.5$	$2.1 \pm 9.8$	$2.9 \pm 8.9$	$-27.9 \pm 6.5$ or $-1.0 \pm 6.7$
$a_2^{(\text{CF})}$ (nHz)	$-6.5 \pm 0.3$	$-6.1 \pm 0.3$	$-17.0 \pm 2.2$	$-15.5 \pm 4.0$
$a_2^{(\text{AR})}$ (nHz)	$86.2 \pm 18.7$	$16.7 \pm 20.4$	$39.0 \pm 20.6$	$34.0 \pm 21.8$
$b(a_2)$ (nHz)	/	/	-10	-10
$b(a_4)$ (nHz)	/	/	-10	-10

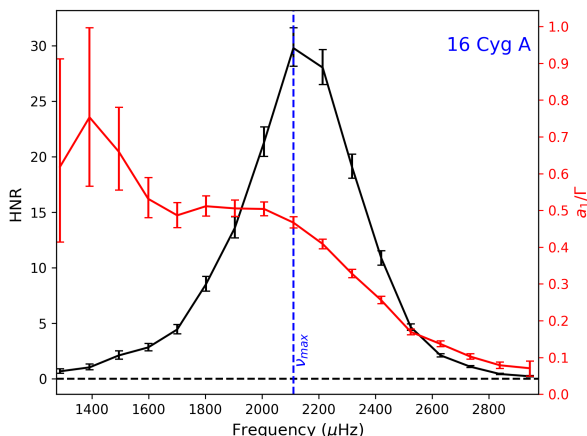


**Fig. 6.** HNR (black) and  $a_1/\Gamma$  ratio (red) for 16 Cyg A, which is the reference star used to make simulations.

is represented as a projected three dimensional vector using the three quantities defined by equation (19) and for  $j \in [1, 2, 4]$ . To evaluate the importance of the bias on  $a_j$ , the plot shows  $b(a_j)/\langle \sigma_{a_j}(i, F) \rangle_i$ , with  $\langle \sigma_{a_j}(i, F) \rangle_i$  the average standard deviation of the probability density functions obtained by the MCMC sampling over  $i \in [30^\circ, 90^\circ]$ . The value of  $\langle \sigma_{a_j}(i, F) \rangle_i$  (noted  $\sigma$  for convenience hereafter) and its variance along the inclination axis is also shown on the plots. A value of  $b(a_j)/\sigma$  greater than one indicates that the inaccuracy exceeds the typical expected uncertainty at  $1\sigma$  and may lead to significantly biased results during the subsequent analyses of the a-coefficients. A negative bias (underestimation) for  $a_j$  is indicated by a cross within the circle while a positive bias (overestimation) by a dot. The darker the colour, the smaller the norm of the normalised bias. The size of the circle symbols is also proportional to the bias, but capped to 3, to avoid excessively large symbols when  $i < 30^\circ$  (see next paragraph for explanations). The case of observations of duration of 2 years are in the top figures (a, b, c) while the 4 years observation case is shown in bottom figures (d, e, f).

We first note that the biases on inclination and on  $F$  are consistent with results from Kamiaka et al. (2018). Regions of stellar inclination below  $30^\circ$  are found to provide very unreliable results and the median of the inclination is biased toward  $\simeq 80^\circ$  when the true input is  $i = 90^\circ$ . Meanwhile, biases in  $a_1$  are found to

often exceed 50% in the gray area<sup>6</sup>, indicating that for inclination below  $\simeq 30^\circ$ , the median estimator of the probability density function might not be trusted. This justifies also the range for the calculation of  $\sigma$ . In the following we therefore focus the discussion of the figures for the region above  $30^\circ$ .

In the case of an equatorial zone of activity, we note that measurements of  $a_1$  may have negligible inaccuracies when the blending factor  $F$  is above 0.4, but starts to be significantly deteriorated at (and probably below)  $f = 0.4$  because  $|b(a_1)|/\sigma$  exceeds 1.5 when  $i < 50^\circ$ . Split components are then overlapping significantly leading to important degeneracies between a-coefficients, mode widths and the stellar inclination. Meanwhile, we note that the biases on  $a_2$  and  $a_4$  remain mild compared to the uncertainty ( $|b(a_2)|/\sigma < 1$  and  $|b(a_4)|/\sigma < 1$ ), even for  $f = 0.4$ .

In the case of a polar active region,  $|a_2|$  represents  $\simeq 20\%$  of the  $a_1$  coefficient. In these conditions, we note that  $b(a_1)/\sigma$  does not exceed the unity (see (a) and (d)), indicating a good accuracy. The terms  $|b(a_2)|/\sigma$  and  $|b(a_4)|/\sigma$  are also lower than 0.5, provided that the stellar inclination is between  $30^\circ$  and  $70^\circ$ . This indicates that a large  $a_2$  coefficient is generally associated with a higher accuracy for all a-coefficients. The plot also demonstrates that a large zone in the parameter space has moderate to small bias.

Interestingly, figures for  $\widehat{HNR}$  of 10 and 20 (Figures D.1-D.4 in Appendix D) lead to similar conclusions. Therefore, even in less favourable  $\widehat{HNR}$  conditions, the expected uncertainty on the measurement generally encompass the bias provided that the stellar inclination exceeds  $\simeq 30^\circ$  (ensuring that  $m \neq 0$  have significant amplitudes) and that the mode blending factor is above 0.4. This indicates that for a majority of stars observed by Kepler, the accuracy may not be a major issue when measuring  $a_1$ ,  $a_2$  and  $a_4$  and provided that a careful assessment of  $F$  and  $i$  is performed. Note however that the average uncertainty  $\sigma$  does usually increase when the  $\widehat{HNR}$  and/or the observation duration decrease, which will have an impact on the precision of the determination of the active region.

## 5. Analysis of solar data

The Sun has a well-known 11-year activity cycle that makes it ideal for testing further the accuracy of the method. The Sun activity cycle is analysed at two instants, highlighted in Figure 2 and for which high-quality helioseismic data are available: (a)

<sup>6</sup>This is likely due to the fit mis-identifying the  $l = 2, m = \pm 1$  with  $l = 2, m = \pm 2$ , effectively doubling or halving the  $a_1$  coefficient.

**Table 3.** Statistical summary for the activity parameters and their model log-marginal likelihood  $\ln(P(\mathbf{O}|\mathbf{M}_{\text{AR}}))$  when  $F(\theta|\mathbf{x}) = \Pi(\theta_0, \delta)$ ,  $\Lambda(\theta_0, \delta)$  or  $N(\theta_0, \delta)$ .  $\ln(P(\mathbf{O}|\mathbf{M}_{\text{CF}}))$  is the log-marginal likelihood for a pure centrifugal effect. The Activity significance is the probability that the activity is necessary to explain the data and derived from the log-marginal likelihoods. Uncertainty on the activity significance is less than 0.25%.

	Active Sun	Quiet Sun	16 Cyg A		16 Cyg B			
	.	.	No bias	bias corr.	No bias	$a_4 \approx -27.9$	$a_4 \approx -1.0$	bias corr.
$\ln(P(\mathbf{O} \mathbf{M}_{\text{CF}}))$	-10.809	-0.367	-1.856	-3.889	-10.596	-1.228	-5.910	-2.951
$\Pi(\theta_0, \delta)$	$\epsilon_{nl} (10^{-4})$	$7.6^{+25.5}_{-5.3}$	$3.7^{+19.6}_{-3.1}$	$5.3^{+19.6}_{-4.1}$	$6.4^{+24.8}_{-4.8}$	$12.5^{+31.9}_{-7.5}$	$4.6^{+20.8}_{-3.7}$	$11.5^{+39.4}_{-7.9}$
	$\theta_0$ (deg)	$76^{+8}_{-7}$	$60^{+19}_{-41}$	$71^{+13}_{-14}$	$79^{+8}_{-10}$	$58^{+3}_{-3}$	$67^{+14}_{-25}$	$61^{+3}_{-4}$
	$\delta$ (deg)	$7^{+16}_{-5}$	$2^{+11}_{-2}$	$4^{+16}_{-3}$	$5^{+15}_{-4}$	$8^{+17}_{-6}$	$3^{+13}_{-2}$	$6^{+14.8}_{-4.6}$
$\ln(P(\mathbf{O} \mathbf{M}_{\text{AR}}))$	-0.685	-0.347	-0.482	-0.656	-0.878	-0.449	-0.781	-0.611
Significance (%)	> 99.99	50.5	79.8	96.2	> 99.9	68.6	99.3	91.2
$\Lambda(\theta_0, \delta)$	$\epsilon_{nl} (10^{-4})$	$14.2^{+33.0}_{-9.8}$	$17^{+42.9}_{-14.2}$	$15.4^{+39.5}_{-12.2}$	$13.6^{+34.1}_{-4.8}$	$21.1^{+35.2}_{-12.6}$	$15.1^{+38.9}_{-12.4}$	$17.3^{+34.0}_{-11.4}$
	$\theta_0$ (deg)	$76^{+9}_{-7}$	$49^{+27}_{-36}$	$66^{+16}_{-41}$	$78^{+21}_{-21}$	$58^{+21}_{-3}$	$58^{+21}_{-40}$	$61^{+3}_{-4}$
	$\delta$ (deg)	$7^{+16}_{-5}$	$6^{+19}_{-5}$	$6^{+17}_{-4}$	$5^{+15}_{-4}$	$10^{+16}_{-6}$	$6^{+17}_{-5}$	$8^{+16}_{-5}$
$\ln(P(\mathbf{O} \mathbf{M}_{\text{AR}}))$	-0.698	-0.296	-0.492	-0.699	-0.930	-0.427	-0.847	-0.639
Significance (%)	> 99.99	51.8	79.6	96.0	> 99.99	69.0	99.4	91.0
$N(\theta_0, \delta)$	$\epsilon_{nl} (10^{-4})$	$3.7^{+16.0}_{-2.2}$	$15.1^{+42.8}_{-13.5}$	$12.2^{+39.5}_{-10.5}$	$6.6^{+24.3}_{-5.0}$	$13.3^{+24.1}_{-7.0}$	$12.6^{+41.0}_{-11.0}$	$6.6^{+24.3}_{-5}$
	$\theta_0$ (deg)	$73^{+11}_{-10}$	$48^{+28}_{-34}$	$63^{+18}_{-38}$	$75^{+11}_{-27}$	$56.6^{+3}_{-7}$	$55^{+23}_{-37}$	$75^{+11}_{-27}$
	$\delta$ (deg)	$9^{+26.6}_{-8}$	$7^{+20}_{-6}$	$6^{+22}_{-5}$	$4^{+20}_{-3}$	$6^{+22}_{-5}$	$7^{+21}_{-6}$	$4^{+20}_{-3}$
$\ln(P(\mathbf{O} \mathbf{M}_{\text{AR}}))$	-0.708	-0.384	-0.584	-0.811	-0.943	-0.516	-0.811	-0.759
Significance (%)	> 99.99	49.6	78.1	95.6	> 99.99	67.1	99.4	90.0
Average	$\epsilon_{nl} (10^{-4})$	$7.7^{+25.7}_{-5.6}$	$11.4^{+41.6}_{-10.0}$	$9.2^{+34.2}_{-7.5}$	$8.0^{+29.4}_{-6}$	$15.5^{+30.7}_{-9.1}$	$10.5^{+37.2}_{-9.0}$	$11.8^{+31.5}_{-7.5}$
	$\theta_0$ (deg)	$75^{+10}_{-8}$	$53^{+25}_{-37}$	$68^{+14}_{-36}$	$78^{+9}_{-14}$	$58^{+3}_{-4}$	$61^{+18}_{-34}$	$60^{+4}_{-6}$
	$\delta$ (deg)	$7^{+22}_{-6}$	$5^{+18}_{-4}$	$5^{+18}_{-4}$	$5^{+17}_{-4}$	$8^{+18}_{-6}$	$6^{+18}_{-5}$	$7^{+19}_{-6}$
$\ln(P(\mathbf{O} \mathbf{M}_{\text{AR}}))$	-0.697	-0.342	-0.519	-0.722	-0.917	-0.464	-0.824	-0.670
Significance (%)	> 99.99	50.6	79.2	96.0	> 99.99	68.2	99.4	90.7

the maximum of activity between January 1999 and January 2002; and (b) the minimum of activity between January 2006 and January 2009. Data are from the Variability of Solar Irradiance and Gravity Oscillations instrument aboard SOHO space-craft (Frohlich et al. 1997) and presents very few gaps.

### 5.1. $a$ -coefficients of the Sun

As for the simulated data, the analysis consists in fitting the power spectrum for cases (a) and (b), to measure the  $a_1$ ,  $a_2$  and  $a_4$  coefficients using the Bayesian modelling and the MCMC method described in the Appendix B. Figures of the best fits and their discussions are provided in Appendix E. The goal being to evaluate the accuracy of the inference of the activity zone from  $a$ -coefficients, the presented results are for a stellar inclination fixed to  $90^\circ$ , instead of having it as a free parameter. This value correspond approximately to the stellar inclination as seen by the SOHO satellite. This alleviates biases on  $a_j$  coefficients that may arise due to the systematic underestimation of  $i$  when it is close to  $90^\circ$  degrees. However, carried tests with a free inclination during the maximum of activity<sup>7</sup> lead to a difference of  $-12\text{nHz}$  in  $a_2$  and to  $-1.3\text{nHz}$  in  $a_4$ . This is consistent with the expected difference from the bias map of Figure 4. In agreement with the discussion of Section 4, the difference does not have a signifi-

cant impact on the activity inference because the uncertainties for those parameters are larger than the observed measurement shift.

Figure 7 shows the measured probability distribution function of the relevant parameters along with their correlations during the maximum of solar activity (left) and the minimum (right). The  $a_2^{(CF)}$  distribution in red represents the expected centrifugal effect on  $a_2$  as derived from frequency shifts  $\delta_{nlm}^{(CF)}$  of equation (13). The distributions are Gaussians and show a weak correlation, reflecting the quality of the data. Between the maximum and the minimum of activity, the  $a_2$  coefficient drifted significantly, from  $a_2 = 80 \pm 19 \text{nHz}$  to  $a_2 = 11 \pm 21$  falling within the  $1\sigma$  confidence interval of the centrifugal term. Although  $a_4$  may have changed, the effect is below uncertainty levels and remain close to 0. As shown in Figure 15, other time intervals may lead to  $a_4$  departing from 0. The figures demonstrate that a comparison of  $a_2$  and  $a_2^{(CF)}$  may reveal the activity of a Sun-like star. At the maximum of activity  $a_2^{(CF)}$  is inconsistent with  $a_2$  at  $4.5\sigma$ , but it is in agreement at  $1\sigma$  during the minimum of activity. Interestingly, Chaplin et al. (2003) also studied in details the frequency asymmetry of  $l = 2$  modes using BiSON and GOLF data with a different methodology, and over period that encompasses the maximum of 1999-2002. Their measure consider only  $T_{n22}$  so a direct comparison is not straightforward. However, we note that with a 844 day-long timeseries starting in

<sup>7</sup>The measured stellar inclination is  $i = 74 \pm 3$  degrees at the maximum of activity of 1999-2002.

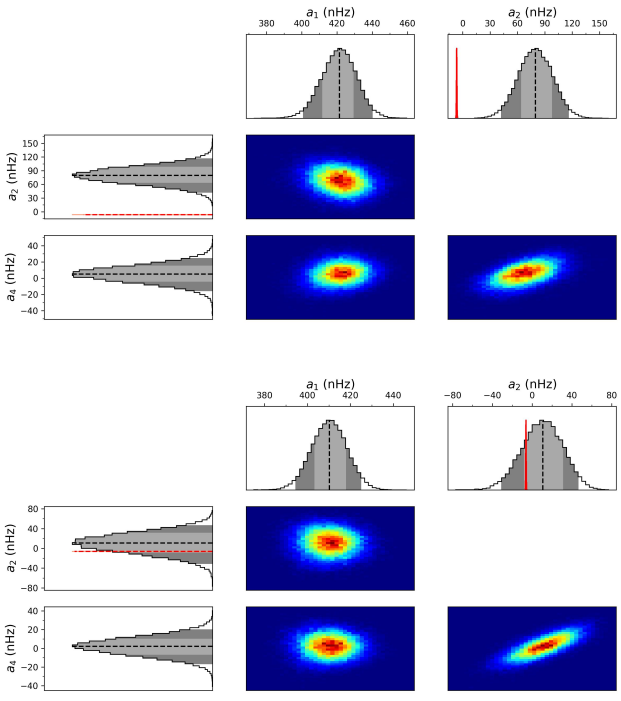


**Fig. 7.** Probability Density Functions and their correlations, obtained by MCMC for coefficients  $a_1, a_2, a_3, a_4$  for the Sun at Maximum of activity (1999-2002, left) and at minimum of activity (2006-2009, right). The red curve is the expected  $a_2^{CF}$  coefficient for a pure centrifugal distortion. The light and dark gray PDF filling is for the  $1\sigma$  and  $2\sigma$  confidence interval, respectively.

Feb 1999<sup>8</sup>, they detect a frequency shift  $T_{n22} \simeq 190$  nHz at a similar significance ( $\simeq 4\sigma$ ) than us when averaging over all modes between  $\simeq 2000 - 3300$   $\mu$ Hz (to be compared to our range of  $\simeq 2300 - 3600$   $\mu$ Hz). Their Figure 8 also show that the global effect of the activity cycle between 1994 and 2000 is evident on the averaged  $T_{n22}$  while the frequency dependence of  $T_{n22}$  may have too large uncertainties to ascertain a frequency-trend. This is in line with our own findings (see our Section 3.3).

A rigorous statistical evaluation of our significance requires the joint use of  $a_2$  and  $a_4$ . This is discussed in Section 5.2, along with other activity results. Finally note that for inclination of  $\simeq 90$  degrees, it is not possible to determine  $a_3$ , because the amplitudes of the azimuthal components for  $l = 1, 2$ , are not favourable (Gizon & Solanki 2004).

## 5.2. Activity of the Sun

The activity intensity and its latitudinal coverage is derived from a fit of the  $a_2^{(AR)}$  and  $a_4^{(AR)}$  coefficients. Technical details are in Appendix C. Statistical summary of the results are listed in Table 3. The statistical significance of the activity exceeds 99.99% (highly significant) at the maximum of activity, but is around 50.6% (not significant) during the minimum of activity, demonstrating the possibility of detecting activity in Sun-like stars. The choice of the function  $F$  describing the active region changes the detection significance by only a few percents. The three explored models fit equivalently the data implying that the shape of the ac-

<sup>8</sup>To be compared to our timeseries of 1095 days starting in Jan 1999.

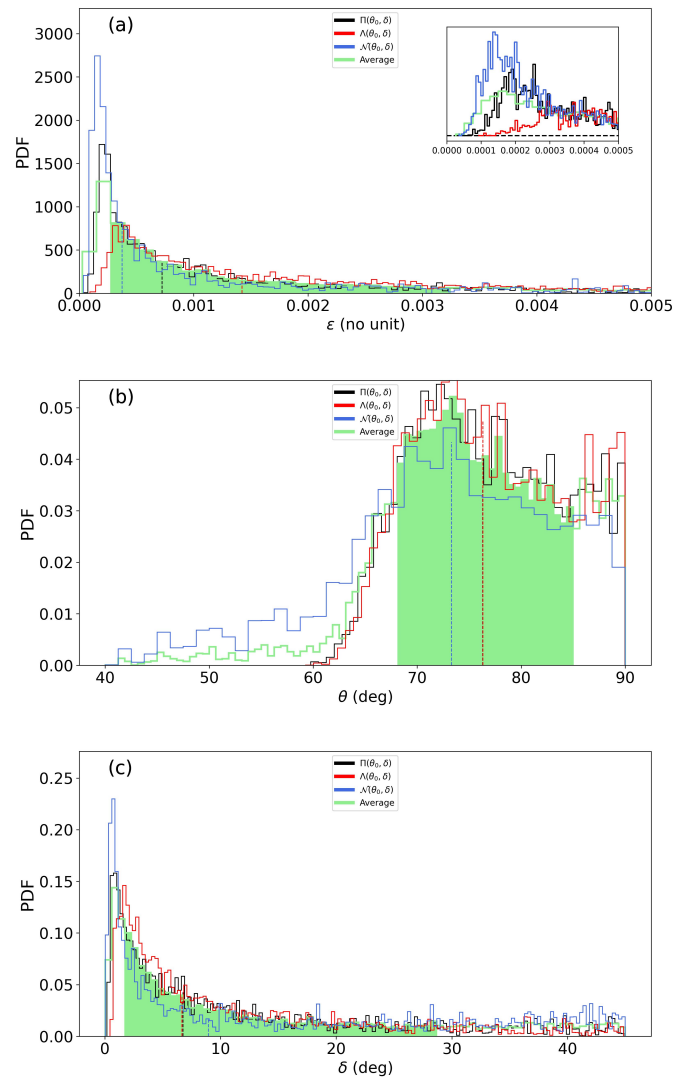


**Fig. 8.** Inferred pdf for (a)  $\epsilon$ , (b)  $\theta_0$  and (c)  $\delta$ , during the Sun maximum activity of 1999-2002. The inset of (a) is a zoom into the near-zero  $\epsilon$  values with smaller binning.

tive region cannot be determined with currently available  $a_2$  and  $a_4$  constraints.

Figure 8 and 9 show  $\epsilon_{nl} = \epsilon, \theta_0$  and  $\delta$  for the Sun at its maximum of activity (1999-2002) and its minimum (2006-2009), respectively. There is no major differences between the three activity profiles, although it is noted that uncertainties are larger in the case of a triangular and a Gaussian activity zone. During the maximum of activity,  $\epsilon \simeq 0$  is clearly excluded (see inset). With  $F = \Pi$ , we observe a log-normal distribution, with median  $7.6 \cdot 10^{-4}$ , consistent with the value reported by Gizon (2002). However, the uncertainty is large, suggesting that only the order of magnitude can be constrained in Sun-like stars. At the minimum of activity, the log-normal distribution morphs into a  $1/x$  law, similar to the Jeffreys prior. This is a sign of weaker statistical significance for the activity.

The co-latitude  $\theta_0 \simeq 75^\circ$  is consistent with the butterfly diagram, which suggests  $\theta_0 \simeq 80^\circ$ . At the minimum of activity and despite a non-significant detection, the probability distribution of  $\theta_0$  shows a weak indication of activity at mid and high co-latitudes. Despite the high significance of the detection during the maximum of activity,  $\delta$  is poorly constrained, showing that

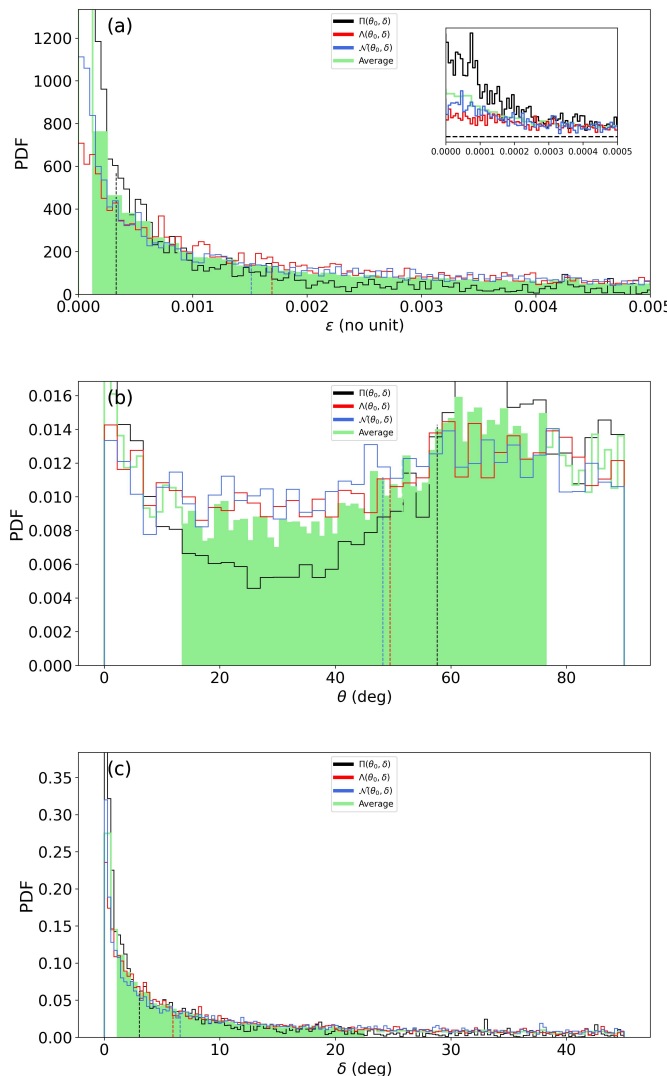


**Fig. 9.** Inferred pdf for (a)  $\epsilon$ , (b)  $\theta_0$  and (c)  $\delta$ , during the Sun minimum activity of 2006–2009. The inset of (a) is a zoom into the near-zero  $\epsilon$  values with smaller binning.

this parameter is challenging to measure on the Sun and on other Sun-like stars.

## 6. Analysis of 16 Cyg A and B

Due to their brightness (magnitudes V=5.95 and 6.20) 16 Cyg A and B have modes with the highest HNR among all of Sun-like stars observed asteroseismically so far. They constitute ideal candidates to evaluate the activity. The two stars are wide binaries, with a confirmed planet around 16 Cyg B (Cochran et al. 1997) and were extensively studied (e.g. Neckel 1986; King et al. 1997; Deliyannis et al. 2000; Schuler et al. 2011; Takeda 2005; Metcalfe et al. 2012; Lund et al. 2014; Verma et al. 2014; Buldgen et al. 2015; Deal et al. 2015; Metcalfe et al. 2016; Roxburgh 2017; Bellinger et al. 2017; Maia et al. 2019; Bazot et al. 2019; Bazot 2020; Farnir et al. 2020; Morel et al. 2021; Buldgen et al. 2022; Nsamba et al. 2022). The 2.5 years (13 September 2010 to 8 March 2013) observation by the Kepler space-borne instrument is used in this section to measure pulsation parameters. The data are the same as those used in Bazot et al.

(2019) for which instrumental issues (outliers, jumps, trends) and the quarter stitching is performed using the procedure described in García et al. (2011a). The binary system has precisely measured angular diameters, making it two of the few Sun-like stars with known interferometric radii. Their measured radius are  $1.22 \pm 0.02R$  and  $1.12 \pm 0.02R$  for 16 Cyg A and B, respectively (White et al. 2013). Their spectroscopic parameters are very close to those of the Sun: Their effective temperatures are  $T_{\text{eff}} = 5825 \pm 50$  K,  $T_{\text{eff}} = 5750 \pm 50$  K and their metallicity are  $[M/H] = 0.10 \pm 0.09$ ,  $[M/H] = 0.05 \pm 0.06$  (Ramírez et al. 2009) for 16 Cyg A and B, respectively. With an estimated age of around 7 Gyrs for both stars (Metcalfe et al. 2016; Bazot 2020, e.g.), they are significantly older than the Sun.

### 6.1. Seismic constraints for 16 Cyg A

Earlier studies of 16 Cyg A revealed around 60 modes of pulsations with significance in the power spectrum<sup>9</sup>. The asteroseismic analysis of Davies et al. (2015) found a stellar inclination of  $56^{+6}_{-5}$  and a rotation  $23.8^{+1.5}_{-1.8}$  ( $\langle \delta\nu_{nlm}/m \rangle_{nl} \simeq 486^{+40}_{-29}$ nHz). Using a refined power spectrum modelling that account for  $a_1$ ,  $a_3$  and parameterises the cavity asphericity  $(R_{\text{eq}} - R_{\text{pol}})/R_{\text{eq}}$ , Bazot et al. (2019) reported values ( $i = 58.5 \pm 6.8$ ,  $a_1 = 464 \pm 43$ nHz), consistent with Davies et al. (2015).

Figure 10 shows the probability density function for  $a_1$ ,  $a_2$ ,  $a_3$  and  $a_4$  for 16 Cyg A, along with their correlation and with  $a_2^{(CF)}$  superimposed in the  $a_2$  quadrant. Table 2 synthesises the inferred values of the coefficients. The probability density functions are near-Gaussian and thus the quadratic mean of the asymmetrical uncertainties is reported in the table. The  $a_1$  coefficient is significantly lower than past estimates but remain consistent at a  $2\sigma$  confidence level. The difference may be due to the lower stellar inclination  $i = 45 \pm 4$ , that is also only consistent with earlier determination at  $2\sigma$ . The  $a_3$  coefficient is marginally greater but with smaller uncertainty than Bazot et al. (2019) (they reported  $a_3 = 11.15 \pm 10.95$ nHz).

More importantly,  $a_2$  is positive at  $1\sigma$ , which is consistent with the assertion of star prolateness from Bazot et al. (2019) and is inconsistent with the centrifugal distortion term,  $a_2^{(CF)}$ . Finally,  $a_4$ , includes zero within  $1\sigma$ .

With respect to Figures 4–5,  $a_1/\Gamma_{\nu_{\text{max}}} = 0.45 \pm 0.04$  and  $i = 45 \pm 4^\circ$  place 16 Cyg A in a parameter space where the expected magnitude of the bias for  $a_1$ ,  $a_2$  and  $a_4$  is of the order of  $0.5\sigma$ ,  $0.5\sigma$  and  $0.8\sigma$  respectively. This remains accurate even when accounting for the slightly higher estimates of inclination from previous publications. Translated into absolute units, this corresponds to approximately  $b(a_1) \simeq +10$ nHz (overestimation),  $b(a_2) \simeq -10$ nHz (underestimation),  $b(a_4) \simeq -10$ nHz (underestimation). These fiducial values are used in Section 6.3 to evaluate the effect of the potential bias on the estimates of the activity zone.

### 6.2. Seismic constraints for 16 Cyg B

Similarly to 16 Cyg A, 16 Cyg B has around 60 observed modes. However, the reported precision for the past determination of the seismic parameters is less accurate than for 16 Cyg A, despite a similar HNR. Davies et al. (2015) and Bazot et al. (2019) both note a large degeneracy between the stellar inclination and the average rotation rate, with even a clear bi-modality in the distributions obtained by Bazot et al. (2019). Their global solution of

<sup>9</sup>The exact value may differ from author to author, due to different choice for the significance.

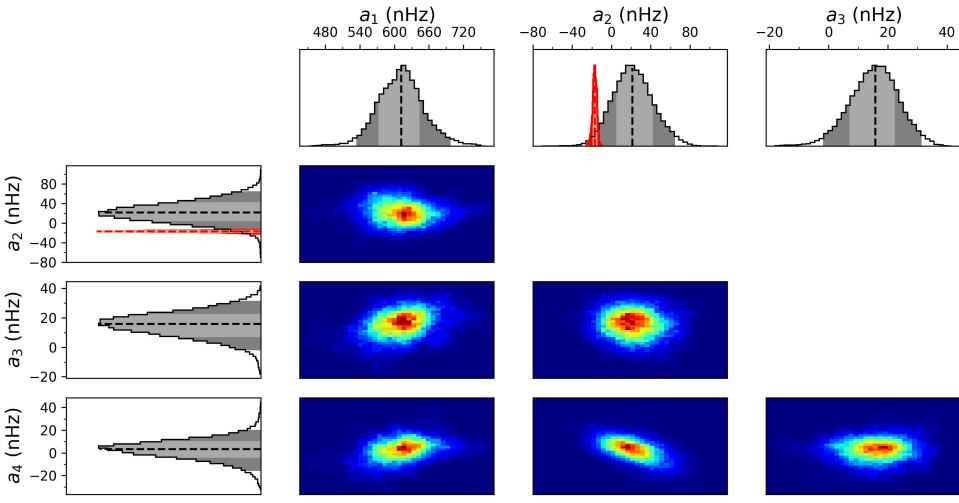


**Fig. 10.** Probability Density Functions and their correlations, obtained by MCMC of the power spectrum of 16 Cyg A and for coefficients  $a_1, a_2, a_3, a_4$  for 16 Cyg A. The red curve shows the expected  $a_2^{CF}$  coefficient for a pure centrifugal distortion of the star. The light and dark gray PDF filling is for the  $1\sigma$  and  $2\sigma$  confidence interval, respectively.

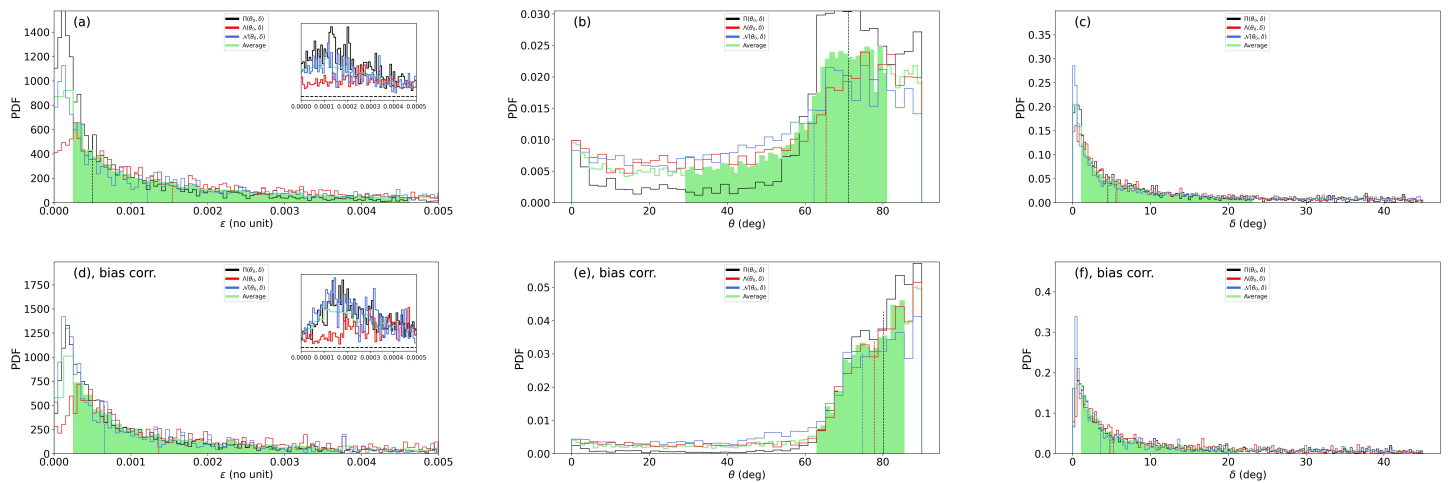


**Fig. 11.** Inferred pdf for 16 Cyg A for raw measures (a,b,c) or with bias correction (d,e,f). The green curve is for the average pdf with  $F = \Pi, \Lambda$  and  $\mathcal{N}$ . The shaded area is its  $1\sigma$  confidence interval. The inset of (a) and (d) is a zoom into the near-zero  $\epsilon$  values with smaller binning.

793  $i = 36_{-7}^{+17}$  is associated with two separate solutions for  $a_1$ , centred around  $\approx 300$ nHz and  $\approx 550$ nHz, that they use to infer the 794 latitudinal differential rotation profile. Meanwhile, as for 16 Cyg 795 A, the star is found to be prolate, indicating a surface activity.

797 Figure 12 shows the measured a-coefficients. It appears that 798 including the  $a_4$  coefficient remove the degeneracy issue ob- 799 served by previous publications. The stellar inclination,  $a_1$  and 800  $a_2$  are precisely determined and have approximately Gaussian 801 probability distributions and these are reported as such in Table 802. The found rotation rate  $a_1$  correspond to the higher solution of 803 rotational splitting of Davies et al. (2015) and Bazot et al. (2019) 804 (see their Figures of probability density functions). Meanwhile, 805 the degeneracy observed in  $a_1$  in earlier studies is moved to  $a_4$ : 806 It exhibits two solutions. As our method of activity inference 807 assumes Gaussian distributions, the bi-modality of  $a_4$  requires 808 to separate the two apparent solutions. Using Gaussian mixture 809 modelling (Bishop 1995; Bazot et al. 2019), the mean and stan-

dard deviation of both solutions are measured, enabling their 810 separate analysis. The lowest estimate ( $a_4 = -27.9 \pm 6.5$ nHz) 811 weights 30% and the highest estimate ( $a_4 = -1.0 \pm 6.7$ nHz) is 812 more significant as it weights 70%. The inference of the activ- 813 ity from the two solutions is discussed in Section 6.4. Note that 814  $a_3 = 45_{-14}^{+13}$ nHz is significantly higher than the reported values 815 from Bazot et al. (2019) ( $a_3 = 13.89 \pm 13.95$ nHz) and may have 816 an impact on the rotational profile. 817

### 6.3. Activity inference for 16 Cyg A

819 Figure 11 shows the results from the inference of the activity pa- 820 rameters and a statistical summary is in Table 3. Triangular and 821 Gaussian descriptions of active latitudes give larger uncertainties 822 than the simple gate model. However, they all suggest a near- 823 equatorial activity, with a similar detection significance level of 824  $\approx 79\%$  (without bias correction) or  $\approx 96\%$  with fiducial corre- 825

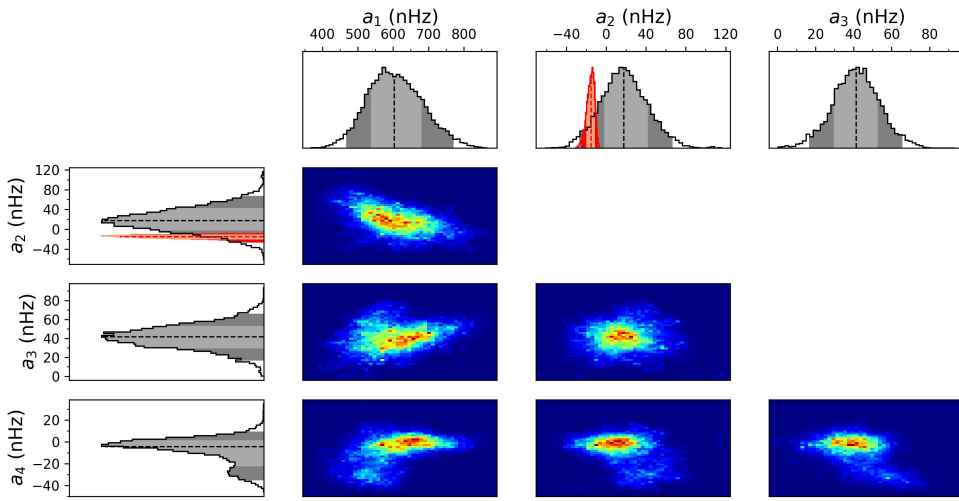


**Fig. 12.** Probability Density Functions and their correlations, obtained by MCMC of the power spectrum of 16 Cyg B and for coefficients  $a_1, a_2, a_3, a_4$  for 16 Cyg A. The red curve shows the expected  $a_2^{CF}$  coefficient for a pure centrifugal distortion of the star. The light and dark gray PDF filling is for the  $1\sigma$  and  $2\sigma$  confidence interval, respectively.

825 tation. As for the Sun and because the shape of the active region  
826 is *a priori* unknown, the average distribution of the parameters  
827 are discussed. The activity intensity has a large uncertainty, but  
828 according to the median of  $\epsilon$ , may be between the maximum and  
829 the minimum of solar activity.

830 The posterior probability distribution of  $\delta$  does not allow us  
831 to precisely constrain the extension of the activity region. As al-  
832 ready noted in the case of the Sun, this parameter requires strin-  
833 gent constraint on both the  $a_2$  and  $a_4$  coefficient in order to in-  
834 form us about the size of the active region.

#### 835 6.4. Activity inference for 16 Cyg B

836 Figure 13 and 14 shows the results for the activity for 16 Cyg  
837 B in the two possible scenarios of  $a_4$  discussed in Section 6.2  
838 (see Table 3 for the statistical summary). In the case of  $a_4 =$   
839  $-27.9 \pm 6.5\text{nHz}$  (Figure 13), the activity is highly significant  
840 (greater than 99.3% with or without bias correction, whatever  
841 is the activity zone model) and has stronger intensity than in the  
842 case of the Sun. The active region is then located at  $\theta_0 \simeq 58^\circ$   
843 ( $\theta_0 \simeq 60^\circ$ , after bias correction), ie. at comparable latitudes seen  
844 during a maximum of activity of the Sun. The bias correction has  
845 negligible effect on the inferred activity latitude. Due to  $a_4$  sig-  
846 nificantly departing from 0, the extension of active region is bet-  
847 ter constrained than in 16 Cyg A or the Sun, but remains weakly  
848 informative.

849 The second more likely solution (probability of 70%) corre-  
850 sponds to  $a_4 = -1.0 \pm 6.7\text{nHz}$  (Figure 14). It is associated to  
851 an activity at co-latitudes above  $\simeq 40^\circ$  and of lower activity. Its  
852 statistical significance is low, and the activity intensity may be  
853 of the same order or lower than 16 Cyg A. In fact, it looks simi-  
854 lar to the solar case when approaching its minimum of activity.  
855 Accounting for the fiducial bias, the solution is more concen-  
856 trated to the equatorial region and differs significantly from the  
857 lower probability  $a_4$  solution. Here, the uncertainty on  $a_2$  and  $a_4$   
858 is again too large to provide a stringent constraint on the exten-  
859 sion of the activity zone  $\delta$ .

## 7. Discussion and Conclusion

The stellar activity is a complex phenomenon emerging from the interplay between the stellar plasma, rotation and magnetism. The activity distorts the shape of mode cavity, perturbing the pulsation frequencies. This perturbation is here observationally evaluated using a  $a$ -coefficient decomposition. This allows us to separate observables (the  $a$ -coefficients) from their physical interpretation (the activity modelling). The separation enables us to demonstrate that the measurements of the average low  $a$ -coefficient,  $a_2$  and  $a_4$ , under some observational conditions, are sufficient to reveal the presence of a statistically significant activity of similar intensity to the Sun and to determine its latitude. The required observational conditions are analysed using a methodology similar to Kamiaka et al. (2018), that is, by constructing a grid of artificial power spectra, that allows us to determine the bias for  $a_1$ ,  $a_2$  and  $a_4$ . It is found that if the height-noise-ratio exceeds 10, the mode blending factor  $f = a_1/\Gamma_{v_{max}}$  is greater than 0.4, the inclination is above  $30^\circ$  and that the observation is longer than 2 years, the inaccuracy remains mild and generally smaller than the  $1\sigma$  uncertainty. The uncertainty and/or the inaccuracy may however become too large to reliably detect any activity beyond the above-specified conditions. In particular and in agreement with Kamiaka et al. (2018), the stellar inclination is a decisive variable to ensure the accuracy of the measurement. Below  $30^\circ$ ,  $a_1$  is often wrong by a factor 2. This is likely due to the fit mistakenly identifying  $l = 2, m = \pm 1$  as  $l = 2, m = \pm 2$  and vice-versa. Other  $a$ -coefficients are then severely inaccurate. Therefore, such a bias analysis suggests that rotation studies of stellar ensembles require a careful star selection.

A method that uses the average  $a_2$  and  $a_4$  coefficients is pro-  
889 posed to perform a subsequent analysis of the activity, consid-  
890 ering a geometrical model of the activity effect on the pulsations  
891 frequencies and accounting for the stellar asphericity due  
892 to the centrifugal effects. This two-step approach is tested on the  
893 case of the Sun and shows that it is effectively able to detect the  
894 change of activity between the solar maximum of activity around  
895 1999-2002 and the minimum of activity around 2006-2009. Al-  
896

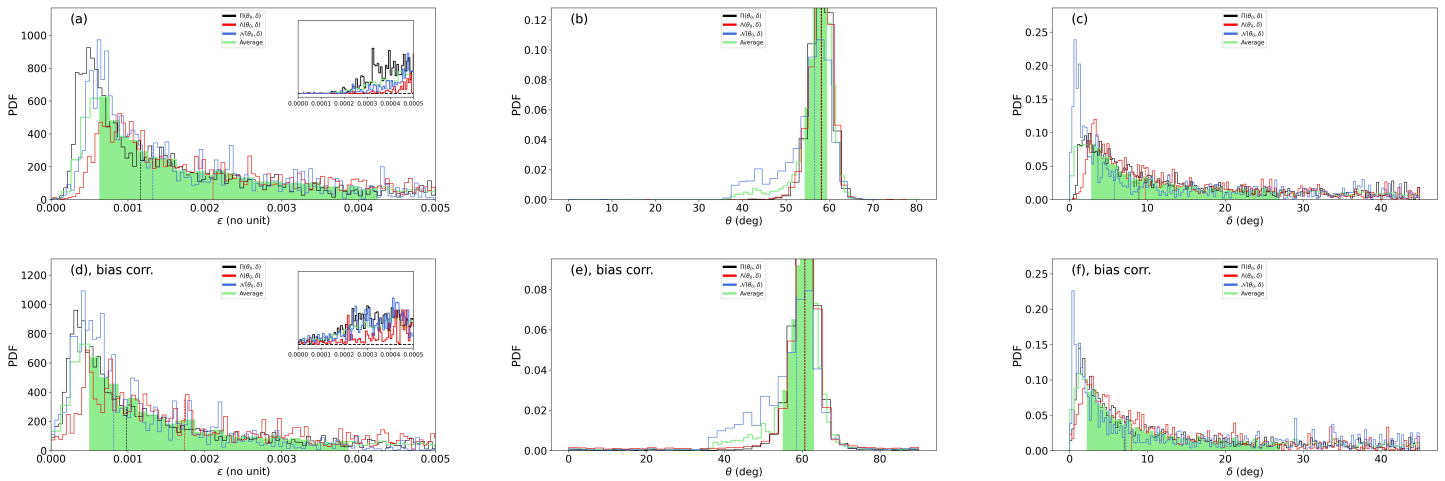


**Fig. 13.** Inferred pdf of  $\epsilon$ ,  $\theta_0$  and  $\delta$  for raw results of 16 Cyg B with the lower solution  $a_4 = -29.2 \pm 5.6\text{Hz}$ , without bias correction (a, b, c) or with it (d, e, f). The green curve is for the average pdf with  $F = \Pi$ ,  $\Lambda$  and  $\mathcal{N}$ . The shaded area is its  $1\sigma$  confidence interval. The inset of (a,d) is a zoom into the near-zero  $\epsilon$  values with smaller binning.

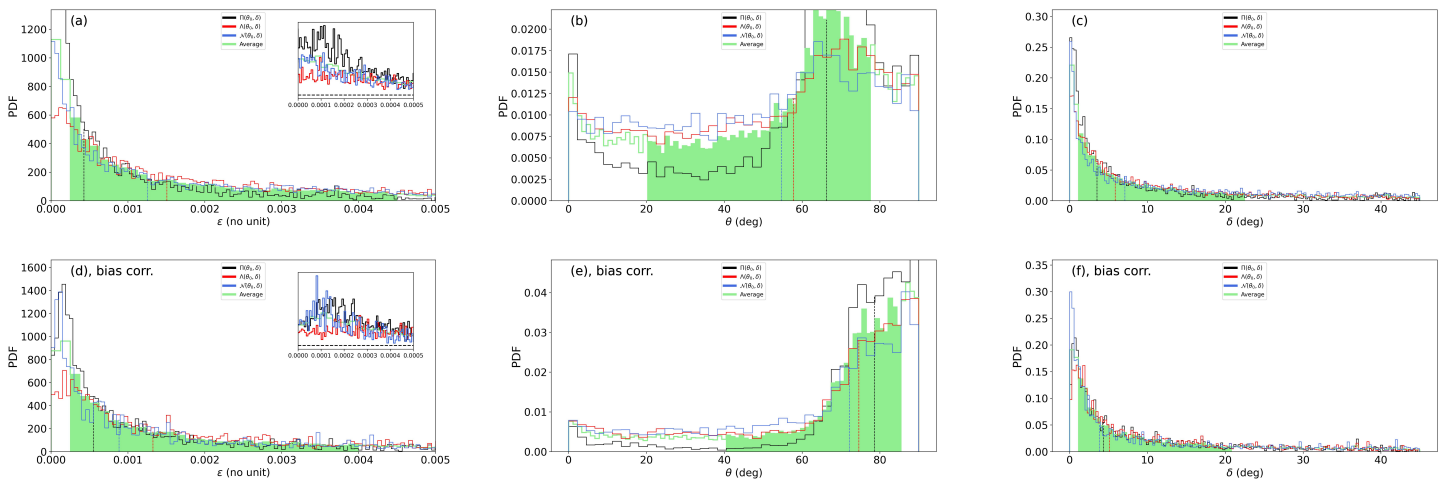


**Fig. 14.** Same as Figure 13 but for the higher solution  $a_4 = -0.9 \pm 6.8\text{Hz}$ .

though the use of averaged a-coefficients makes it difficult to evaluate the extension of the activity zone, the model successfully retrieves the mean latitude of activity during the maximum of the solar cycle.

The method is then applied to the brightest stars observed during the initial observational phase of the Kepler space instrument, 16 Cyg A and B. These stars were selected as a test-bed due to the fact that they are well studied and present the highest mode signal-to-noise ratio of all the currently known main-sequence stars. Davies et al. (2015) suggested that these stars have mild to no activity. However, Bazot et al. (2019), using a parametric model for describing the asphericity ( $R_{\text{eq}} - R_{\text{pol}})/R_{\text{eq}}$ ) found an asphericity significant at  $1\sigma$ . Our current analysis, performed using the same data set, confirms this asphericity and found a mild (relatively to the Sun) to moderate activity for both stars. It is found that 16 Cyg A has a near-equatorial band of activity during the period of observation (13 September 2010 to 8 March 2013), with a significance of the detection greater than 79.8%.

The case of 16 Cyg B is more ambiguous. A bi-modality on the average splitting  $\langle \delta v_{nlm} / m \rangle \simeq a_1$  and on the stellar inclination is already reported in Davies et al. (2015) and Bazot et al. (2019).

Our refined model suggests that this bi-modality is in fact related to the  $l = 2$  modes. Indeed, as we account for  $a_1$ ,  $a_2$ ,  $a_3$  and  $a_4$ , we note that the bi-modality previously seen on  $a_1$  in earlier studies is displaced to  $a_4$ . The solutions of  $a_4$  are separated using a Gaussian process algorithm, which found that the weight (or importance) of the highest solution, close to 0 nHz is of 70%. The lower solution, close to -28nHz has a weight of 30%. The associated probability distribution for stellar inclination  $i = 35 \pm 3$  is unique (instead of being bi-modal in past studies). The two solutions of  $a_4$  are analysed independently. The lower solution (with lower weight) is associated to an overall activity that is stronger than the Sun, localised at latitudes of approximately 32° (with an uncertainty of  $\simeq 3^\circ$ ). The higher solution is linked to a lower activity and is weakly significant (probability greater than 67.1%). Although the uncertainty is large, the study suggests an activity closer to the equatorial region. In the Sun and as evident in its butterfly diagram, the quiet phase is associated to a magnetic activity closer to the equator, while the transition to the active Sun is abrupt and characterised by the appearance of magnetic spots at latitudes of 30–40°. In that context and although it is not possible to rule out the possibility of a statistical fluke, an interpretation of the bi-modality is that the star was transitioning from a

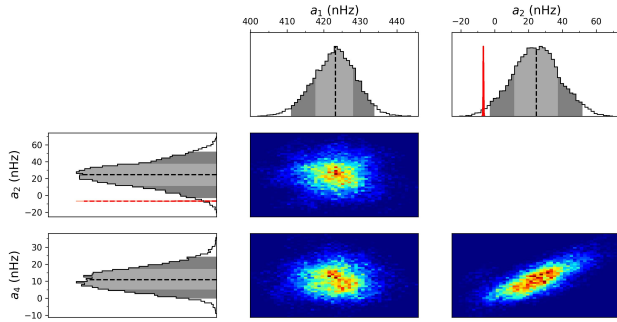


**Fig. 15.** Probability Density Functions and their correlations, obtained by MCMC for coefficients  $a_1, a_2, a_3, a_4$  for the Sun in-between two activity cycles (2006-2011). The red curve is the expected  $a_2^{CF}$  coefficient for a pure centrifugal distortion. The light and dark gray PDF filling is for the  $1\sigma$  and  $2\sigma$  confidence interval, respectively.

941 period of low activity to a more active period during the observa-  
 942 tion time of the Kepler instrument. To evaluate that hypothesis,  
 943 we selected solar-data between Jan 2006 and Jan 2011, includ-  
 944 ing the end of a cycle and the start of a new one. The measured  
 945 a-coefficients for that analysis are shown in Figure 15. There is  
 946 no visible bi-modality on either  $a_2$  or  $a_4$ . Because 16 Cyg B is  
 947 evidently different than the Sun, this does not refute the hypoth-  
 948 esis, but weakens it. A more firm verification would require a  
 949 follow-up observation of the star, ie with PLATO (Rauer et al.  
 950 2014). Or extensive simulations in order to attempt to reproduce  
 951 the bi-modality.

952 This work demonstrates that it is possible to determine the  
 953 latitude and intensity of the activity for Sun-like stars, when this  
 954 activity is similar to, or exceed the one of the Sun. The lim-  
 955 ited observed bias suggests that the analysis of the stellar ac-  
 956 tivity could also be extended to a larger set of stars. The Kepler  
 957 LEGACY stars (Lund et al. 2017) are ideal candidates as these  
 958 generally satisfy the criteria of reliability that are discussed in  
 959 this conclusion and detailed in Section 4.

960 Although the a-coefficient analysis has the benefit to allow  
 961 to simplify the bias studies and to make the analysis faster, a fur-  
 962 ther axis of improvement would consist in using a single analysis  
 963 step, ie, fitting directly the power spectrum with the model of ac-  
 964 tivity. Contrary to the two-step analysis, such an approach does  
 965 not require assumptions on the properties of probability distribu-  
 966 tion of the a-coefficients as it is currently the case. It would also  
 967 make use of the full set of a-coefficients (not only their average),  
 968 which may lead to smaller uncertainties. However, the two ap-  
 969 proaches would certainly be needed in tandem, as the stability  
 970 of the solution (and its accuracy) is harder to ascertain when  
 971 performing a single step fitting approach.

972 O.B. and L.G. acknowledge partial support from NYUAD  
 973 Institute Grant G1502 "Center for Space Science". L.G. is  
 974 supported in part by the European Research Council (ERC)  
 975 Synergy Grant WHOLE SUN 810218 and the Max Planck  
 976 Society grant "Preparations for PLATO Science". We thank  
 977 Saskia Hekker for comments and advice. All data presented  
 978 in this paper were obtained from the Mikulski Archive for  
 979 Space Telescopes (MAST) at the Space Telescope Science In-  
 980 stitute. The specific observations analysed can be accessed via  
 981 [10.17909/T9059R]<https://doi.org/10.17909/T9059R>.

982 SOHO spacecraft, Kepler spacecraft

## 985 Appendix A: Polynomials, a-coefficients and 986 splittings

### 987 A.1. The first six used polynomials

988 The  $\mathcal{P}_j^{(l)}(m)$  coefficients, which are introduced by Schou et al.  
989 (1994), can be obtained by normalising the  $H_j^m(l)$  coefficients by  
990 Ritzwoller & Lavelle (1991) so that  $\mathcal{P}_j^{(l)}(m = l) = l$ .

$$\begin{aligned} \mathcal{P}_j^{(l)}(m) &= \frac{l(2l-j)!}{(2l)!} H_j^m(l) \\ &= (-1)^{-l+m} \frac{l \sqrt{(2l-j)!(2l+j+1)!}}{(2l)!} \begin{pmatrix} j & l & l \\ 0 & m & -m \end{pmatrix} \end{aligned} \quad (\text{A.1})$$

991 in which the last factor means the Wigner 3j symbol.

992 They can also be obtained by recurrence using equation (2)  
993 and (3), together with the normalisation condition,  $\mathcal{P}_j^l(m) = l$   
994 and starting with  $\mathcal{P}_0^l(m) = l$ .

995 The first six polynomials are as follows:

$$\mathcal{P}_1^{(l)}(m) = m \quad (\text{A.2})$$

$$\mathcal{P}_2^{(l)}(m) = \frac{3m^2 - l(l+1)}{2l-1} \quad (\text{A.3})$$

$$\mathcal{P}_3^{(l)}(m) = \frac{5m^3 - (3l(l+1)-1)m}{(l-1)(2l-1)} \quad (\text{A.4})$$

$$\mathcal{P}_4^{(l)}(m) = \frac{(35m^4 - 5(6l(l+1)-5)m^2) + 3l(l+1)(l(l+1)-2)}{2(l-1)(2l-1)(2l-3)} \quad (\text{A.5})$$

$$\mathcal{P}_5^{(l)}(m) = \frac{252m^5 - 140(2L-3)m^3 + (20L(3L-10)+48)m}{8(4l^4 - 20l^3 + 35l^2 - 25l + 6)} \quad (\text{A.6})$$

$$\begin{aligned} \mathcal{P}_6^{(l)}(m) &= \frac{924m^6 - 420m^4(3L-7) + 84m^2(5L^2 - 25L + 14)}{N} \\ &\quad - \frac{20L(L^2 - 8L + 12)}{N} \end{aligned} \quad (\text{A.7})$$

1000 where  $L = l(l+1)$  and  $N = 64l^5 - 480l^4 + 1360l^3 - 1800l^2 +$   
1001  $1096l - 240$ .

### 1002 A.2. Relationship between a-coefficients and splittings

1003 The relationships between a-coefficients and symmetric/anti-  
1004 symmetric splittings can be derived using equations (4) and  
1005 (5). These are used to convert model frequencies  $\nu_{nlm}$  into a-  
1006 coefficients.

#### 1007 A.2.1. Explicit form for low a-coefficients and l=1

$$a_1(n, l = 1) = S_{n11} = \frac{\nu_{n,1,1} - \nu_{n,1,-1}}{2} \quad (\text{A.8})$$

$$a_2(n, l = 1) = T_{n11}/3 = \frac{(\nu_{n,l,-1} + \nu_{n,l,1})/2 - \nu_{n,l,0}}{3} \quad (\text{A.9})$$

### A.2.2. Explicit form for low a-coefficients and l=2

$$a_1(n, l = 2) = \frac{S_{n21} + 4S_{n22}}{5} \quad (\text{A.10})$$

$$a_2(n, l = 2) = \frac{2T_{n22} - T_{n21}}{7} \quad (\text{A.11})$$

$$a_3(n, l = 2) = \frac{S_{n22} - S_{n21}}{5} \quad (\text{A.12})$$

$$a_4(n, l = 2) = \frac{T_{n22} - 4T_{n21}}{70} \quad (\text{A.13})$$

### A.2.3. Explicit form for low a-coefficients and l=3

$$a_1(n, l = 3) = \frac{S_{n31} + 4S_{n32} + 9S_{n33}}{14} \quad (\text{A.14})$$

$$a_2(n, l = 3) = \frac{-15T_{n31} + 25T_{n33}}{126} \quad (\text{A.15})$$

$$a_3(n, l = 3) = \frac{-S_{n31} - 2S_{n32} + 3S_{n33}}{9} \quad (\text{A.16})$$

$$a_4(n, l = 3) = \frac{T_{n31} - 7T_{n32} + 3T_{n33}}{77} \quad (\text{A.17})$$

$$a_5(n, l = 3) = \frac{5S_{n31} - 8S_{n32} + 3S_{n33}}{126} \quad (\text{A.18})$$

$$a_6(n, l = 3) = \frac{15T_{n31} - 6T_{n32} + T_{n33}}{1386} \quad (\text{A.19})$$

## Appendix B: Spectrum analysis

### B.1. Acoustic-spectrum modelling

The analysis of the asteroseismic data is very often performed by fitting the power spectrum (eg. Appourchaux et al. 1998, 2008). This requires to devise a likelihood function and a model for the observed spectrum. As our fitting involves a Bayesian approach, the priors are also required.

#### B.1.1. Likelihood

The likelihood function is determined by the noise statistics of the power spectrum, which is a  $\chi^2$ -squared with two degree of freedom. It is also based on the assumption that the frequency bins are independent and uncorrelated. This implies that the observation duration is assumed to be much greater than the typical lifetime of the pulsation modes and that the duty cycle is sufficient to allow us to neglect any leakage induced by the window function. The observation timeframe for the LEGACY sample is of the order of years, which is significantly longer than the mode lifetime. Furthermore, the duty cycle is above 95%, which

1037 was shown to be sufficient to neglect leakage (Stahn 2010). Under these conditions, the likelihood function is (Anderson et al.  
1038 1990),  
1039

$$L_1(S(\nu_i)|X, M) = \sum_{i=0}^{N-1} \frac{1}{S(\nu_i)} \exp\left(-\frac{S(\nu_i)}{M(\nu_i, X)}\right) \quad (\text{B.1})$$

1040 where  $S(\nu_i)$  is the power at the central frequency  $\nu_i$  of the  $i^{\text{th}}$  bin.  
1041 Here,  $N$  is the total number of bins and  $M(\nu_i, X)$  is the model of  
1042 the power spectrum with the set of variable  $X$  for the model  $M$ .

1043 From Bayes theorem, the posterior probability density function  
1044 is defined as,

$$\pi_1(X|S(\nu), M) = \frac{\pi_1(X|M) L_1(S(\nu)|X, M)}{\pi_1(S(\nu)|M)} \quad (\text{B.2})$$

1045 where  $\pi_1(X|M)$  is the prior knowledge on the parameters  $X$ .  
1046  $\pi_1(S(\nu)|M)$  is a normalisation constant, essential only for com-  
1047 paring the significance of models (eg. Gregory 2005; Benomar  
1048 et al. 2009). Variables are assumed to be independent from each  
1049 others. This implies that the joint prior is the product of individ-  
1050 ual priors. The posterior is evaluated using the Tempered Adap-  
1051 tive MCMC code<sup>10</sup> described in Atchadé (2006) and imple-  
1052 mented by Benomar (2008).

### 1053 B.1.2. Acoustic spectrum model

1054 The model used for the power spectrum fitting, involves a sum  
1055 of asymmetrical Lorentzian, superimposed to a monotonically  
1056 decreasing function of frequency (pink noise). The asymmet-  
1057 ric Lorentzian is commonly used in helioseismology (Duvall  
1058 et al. 1993; Nigam & Kosovichev 1998; Georgobiani et al. 2000;  
1059 Toutain et al. 1998) and in asteroseismology for Sun-like stars  
1060 (Benomar et al. 2018b),

$$M(\nu) = \sum_{n=n_0}^{n_{\max}} H_{nlm} \frac{(1 + B_{nlm} z)^2 + B_{nlm}^2}{1 + z^2} + N(\nu), \quad (\text{B.3})$$

1061 with  $z = 2(\nu - \nu_{nlm})/\Gamma_{nlm}$ . Each asymmetrical Lorentzian is  
1062 defined by a height  $H_{nlm}$ , width  $\Gamma_{nlm}$ , a central frequency  $\nu_{nlm}$   
1063 and an asymmetry  $B_{nlm}$ . As explained by Gizon (2006); Beno-  
1064 mar et al. (2018b), the asymmetry coefficient depends on the  
1065 mode width and frequency. The normalised asymmetry coeffi-  
1066 cient  $\chi_{nlm} = 2 \frac{B_{nlm} \nu_{nlm}}{\Gamma_{nlm}}$  is fitted instead as it is nearly constant over  
1067 the range of fitted modes.

1068 Several prescriptions exist for describing the noise back-  
1069 ground  $N(\nu)$ . Here, it is assumed to be a sum of two generalised  
1070 Lorentzian, sometimes referred as Harvey-like profiles (Harvey  
1071 1985), and of a white noise,

$$N(\nu) = \frac{A_1}{1 + (\tau_1 \nu)^{p_1}} + \frac{A_2}{1 + (\tau_2 \nu)^{p_2}} + N_0. \quad (\text{B.4})$$

1072 Here  $N_0$  is the white noise and  $A_k$  is the maximum heights of the  
1073  $k^{\text{th}}$  generalised Lorentzian. The  $\tau_k$  parameter is timescale that is  
1074 the inverse of the full width at half maximum of the Lorentzians,  
1075 and  $p_k$  is a power exponent.

1076 The fit is performed globally over all the statistically sig-  
1077 nificant peaks visible in the power spectrum of a star. This can  
1078 lead to a very large number of fitted parameters (up to a few  
1079 thousands), which is practically unsuitable. A model simplifi-  
1080 cation is therefore preferred, similar to eg. Appourchaux et al.  
1081 (2008); Benomar et al. (2009); Campante et al. (2011); Handberg  
1082 & Campante (2011) with main simplifications recalled hereafter,

- The  $m$  dependence on heights is controlled by its relation-  
1083 ship with the stellar inclination (Gizon & Solanki 2003). This  
1084 saves several hundreds of parameters.
- The relative height of the different degree  $l$  is constant across  
1085 the fitted range and for a given  $l$ , hence  $V_l^2 = H_{n,l}/H_{n,l=0} =$   
1086 *const.* Only the  $l = 0$  heights  $H_{n,l=0}$  are variables. The mode  
1087 visibility  $V_l^2$  replaces the  $H_{n,l>0}$  as a variable.
- Given a degree  $l$ ,  $\Gamma_{n,l,m} = \Gamma_{n,l}$  is imposed. This is justified by  
1090 the fact that the width depends weakly on the frequency: all  
1091 split components are assumed to have the same width.
- Because  $\Gamma_{n,l}$  is nearly independent of the degree, it is possi-  
1093 ble to fit  $\Gamma(\nu) = \Gamma_{n,l=0}$  and interpolate it to the frequencies of  
1094 the modes with degree  $l > 0$ .

These assumptions reduce the number of variables to a few tens  
1096 in the case of CoRoT, Kepler or TESS observations. The fre-  
1097 quencies of the modes follow equation (14) in Section 2.3.

### 1099 B.2. Priors

Priors are fundamental of a Bayesian method. This section ex-  
1100 plicits  $\pi_1(X|M, I)$ , the prior used during the power spectrum fit-  
1101 ting. Parameters of the vector  $X$  are assumed independent to each  
1102 others, such that the product rule is used to define  $\pi_1(X|M, I)$ .

Heights, widths, frequencies, asymmetry and inclination  
1104 use non-informative priors. These are either Jeffreys priors for  
1105 scale parameters, noted  $\mathcal{J}(x_{\min}, x_{\max})$  or uniform prior, noted  
1106  $\mathcal{U}(x_{\min}, x_{\max})$ . Priors on frequencies are uniform and require a  
1107 visual inspection of the power spectrum in order to assign the  
1108 lower and upper bound of the prior for each mode that follow  
1109 the expected pattern for main sequence Sun-like stars (equally  
1110 spaced p modes) and that show an excess of power relative to  
1111 the background that exceeds 80%. The excess of power is deter-  
1112 mined using a smooth spectrum for which the noise statistics is  
1113 derived by Appourchaux (2003). Mode visibilities are defined by  
1114 Gaussian priors (noted  $\mathcal{G}(x_0, \sigma)$ ), with mean  $x_0$  set as the solar  
1115 value (see Ballot et al. 2011) and the standard deviation  $\sigma$  is 10%  
1116 of the mean. Table B.1 lists the type and the prior characteristic  
1117 values that are used for the parameters of the modes.

The prior on  $a_1$  is uniform between 0 and 1500 nHz. For  
1119 16 Cyg A and B, an uniform fixed prior is set on  $|a_3|$  over the  
1120 range [0, 100] nHz. However at each iteration of the optimisa-  
1121 tion process,  $|a_3|$  is not allowed to exceed 20% of  $a_1$ . Preventing  
1122 extremely large relative value of  $a_3/a_1$ , improves the fit stability  
1123 and ensure a faster convergence of the algorithm. For the Sun  
1124 analysis and because it is not possible to measure  $a_3$  for  $i \approx 90^\circ$   
1125 (due to the lack of amplitude of  $l = 2, m = \pm 1$  at that inclination),  
1126  $a_3$  is fixed to 0.

The priors on  $a_2$  and  $a_4$  are also uniform. The range is defined  
1128 by using the maximum range of Figure 3 (showing  $a_2^{(AR)}$  and  
1129  $a_4^{(AR)}$ ), increasing it by 50% and adding the expected centrifugal  
1130 term  $a_2^{(CF)}$ , assuming  $a_1 = 400$ nHz for the Sun and  $a_1 = 600$ nHz  
1131 for 16 Cyg A/B. The  $\Delta\nu$  reported in Table 2 is also used. For the  
1132 same reason as to  $a_3$ ,  $a_2/a_1$  cannot exceed 50% and  $a_4/a_1$  cannot  
1133 exceed 20% at each iteration step of the optimisation process.

The noise priors are obtained from a global MAP approach  
1135 similar to Benomar et al. (2012). This provides the best fit val-  
1136 ues and  $1\sigma$  uncertainties that are used as priors. The noise back-  
1137 ground of the individual model analysis is described by equation  
1138 (B.4). During the global MAP fit, the model is made of that same  
1139 background model, plus a Gaussian envelope to account for the  
1140 power excess due to the modes (eg Mathur et al. 2010; Huber  
1141 et al. 2011).

<sup>10</sup><https://github.com/OthmanB/Benomar2022/Programs/TAMCMC-1.81>

**Table B.1.** Mode priors used for the fit of the power spectrum. Prior parameters on frequencies are visually determined, see Section B.2.

Main mode parameters						
Height ( $\text{ppm}^2/\mu\text{Hz}$ )	Width ( $\mu\text{Hz}$ )	Frequency ( $\mu\text{Hz}$ )	Asymmetry ( $ \chi $ )	$V_{l=1}^2$	$V_{l=2}^2$	inclination
$\mathcal{J}(1,1000)$	$\mathcal{J}(0.1, 45)$	$\mathcal{U}(\nu_{\min}, \nu_{\max})$	$\mathcal{J}(5, 100)$	$\mathcal{G}(1.5, 0.15)$	$\mathcal{G}(0.53, 0.053)$	$\mathcal{U}(0,90)$

## Appendix C: Inference of the active latitudes

The determination of the activity is performed as a second step using as observables the marginalised posterior distribution of the average a-coefficients. This section describes the method and assumptions to determine the posterior distribution and to compute the significance of the detection.

### C.1. Posterior distribution and likelihood

Similarly as to the power spectrum fitting described in Section B, the determination of the most likely latitudes for the activity and its significance necessitate the computation of a posterior distribution,

$$\pi_2(X|\mathbf{O}, M) = \frac{\pi_2(X|M) L_2(\mathbf{O}|X, M)}{\pi_2(\mathbf{O}|M)}, \quad (\text{C.1})$$

with  $\pi_2(X|\mathbf{O}, M)$ ,  $\pi_2(X|M)$ ,  $L_2(\mathbf{O}|X, M)$  are the posterior distribution, the prior, the likelihood, respectively. The denominator  $\pi_2(\mathbf{O}|M)$  is the normalisation constant used for model comparison (marginal likelihood). The posterior distributions of the a-coefficients  $a_{2,o}$  and  $a_{4,o}$  obtained by power spectrum fitting are the observables contained in  $\mathbf{O}$ . The class of the model is identified by the variable  $M$ .

For simplicity, the observables are assumed to be distributed according to un-correlated Gaussian functions, such that  $\mathbf{O} = \{a_{2,o}, a_{4,o}, \sigma_{2,o}, \sigma_{4,o}\}$ , where  $a_{2,o}$  and  $a_{4,o}$  are the mean for the distributions of  $a_2$  and  $a_4$  while  $\sigma_{2,o}$ ,  $\sigma_{4,o}$  are the standard deviations. This leads to a log-Likelihood in the form of a  $\chi^2$ -squared,

$$\ln L_2(X|\mathbf{O}, M) = -\frac{(a_{2,o} - a_{2,m}(X))^2}{2\sigma_{2,o}^2} - \frac{(a_{4,o} - a_{4,m}(X))^2}{2\sigma_{4,o}^2}. \quad (\text{C.2})$$

In Dziembowski et al. (2000), a-coefficients are weighted using the inverse of the mode inertia (see their equation 4). This is due to the fact that the inertia account for most of the frequency-variations of the coefficients. It is essentially relevant if the uncertainties are small enough to observe a trend when modes are fitted individually. However, in the case of the Sun and with either GOLF or BiSON data, it is difficult to perceive a frequency-trend (Chaplin et al. 2003). Our own trials on VIRGO/SPM using a linear fit to describe the frequency dependence of a-coefficient did not detect a slope that is significant at more than  $1\sigma$ . A similar analysis on 16 Cyg A and B and on simulations showed evidence of large uncertainties when attempting to determine frequency-variations for stars with HNR typical of Kepler observations. In fact, only the average the a-coefficient over  $l$  and  $n$  is shown to be robustly determined (see also our discussion Section 3.3) so that inertia effects are here neglected.

The activity model  $M_{AR}$  depends on the variables  $X = \{\epsilon, \theta_0, \delta\}$  and  $a_{2,m}(X), a_{4,m}(X)$  denote the modelled a-coefficients.

The log-likelihood is then,

$$\begin{aligned} \ln L_2(a_{2,o}, a_{4,o}, \sigma_{2,o}, \sigma_{4,o}|a_{2,m}, a_{4,m}, M_{AR}) = \\ -\frac{(a_{2,o} - a_{2,m}(\epsilon, \theta_0, \delta))^2}{2\sigma_{2,o}^2} \\ -\frac{(a_{4,o} - a_{4,m}(\epsilon, \theta_0, \delta))^2}{2\sigma_{4,o}^2}. \end{aligned} \quad (\text{C.3})$$

In our case, the observables are the average of the fitted modes coefficients,  $a_{2,o} = a_2^{(CF)} + a_2^{(AR)}$  and  $a_{4,o} = a_4^{(AR)} = 0$ . However, to conveniently propagate all errors on the parameters of  $a_2^{(CF)}$  ( $a_1, \Delta\nu, \Delta\nu_\odot, \rho_\odot, \nu_{nl}$ ), it is preferable to use  $a_{2,o} = a_2^{(AR)}$ , obtained by subtracting the  $a_2^{(CF)}$  from the  $a_2$  measured by power spectrum fitting. The distribution of  $\Delta\nu$  is computed by linear fitting of the group-wise ensemble of samples  $(n, l = 0)$  for each measured frequencies  $\nu_{nl}$ . The term  $a_2^{(CF)}$  is finally obtained by weighted average of all independent  $a_2^{(CF)}(n, l)$  computed at the star's posterior frequencies  $\nu_{nl}$ . The subtraction of  $a_2^{(CF)}$  is then again performed using the samples of its posterior, enabling to construct of the posterior probability distribution function of  $a_2^{(AR)}$ , from which we deduce its mean  $a_{2,o}$  and its standard deviation  $\sigma_{2,o}$ . To evaluate the relevance of the activity, two models are considered. First, a model ( $M = M_{CF}$ ) without activity, that accounts only for the centrifugal effects and second, a model ( $M = M_{AR}$ ) with activity. Their details and the choice of the priors is described in the following sections for each of them.

### C.2. Model without activity $M_{CF}$

The model  $M_{CF}$  has no unknown variable that require minimisation, see equation (13). For the sake of the model comparison with the model  $M_{AR}$ , it is however important to determine the marginal likelihood of  $M_{CF}$ . From that perspective, it is necessary to calculate the denominator of equation (C.1),  $P(\mathbf{O}|M_{CF})$  which is defined as an integral,

$$P(\mathbf{O}|M_{CF}) = \int \pi(X|M_{CF}) L_2(\mathbf{O}|a_{2,m}, a_{4,m}, M_{CF}) dX. \quad (\text{C.4})$$

An absence of activity correspond to the limit case where the a-coefficients of the activity are exactly 0. This corresponds to setting Dirac priors on  $a_{2,m} = \delta_0$  and  $a_{4,m} = \delta_0$  and implies that the marginal likelihood is the local value of the likelihood at  $X = \{0, 0\}$ . The model comparison is commonly performed in log-space such that,

$$\ln P(a_{2,o}, a_{4,o}, \sigma_{2,o}, \sigma_{4,o}|M_{CF}) = -\frac{a_{2,o}^2}{2\sigma_{2,o}^2} - \frac{a_{4,o}^2}{2\sigma_{4,o}^2}. \quad (\text{C.5})$$

### C.3. Model with activity $M_{AR}$

Regarding the model with activity of equation (C.3), priors must then be set on the variables subject to optimisation. The  $\epsilon$  and  $\delta$

parameters are indispensable intensive parameters and the adequate non-informative prior is then the (truncated) Jeffreys prior (Jeffreys 1961), uniform in the log-space,

$$J(x) = \frac{\ln(1 + x_{max}/x_{min})}{x + x_{min}}, \quad (\text{C.6})$$

where  $x_{min}, x_{max}$  are upper and lower bounds such that if  $x > x_{max}$  or  $x < x_{min}$  then  $J(x) = 0$ . This guarantees that the probability density is proper (the integral over  $x$  is finite). In case of weak information content in the observables, this prior is more weighted toward a null-value. We set  $\epsilon_{min} = 5 \cdot 10^{-4}$  and  $\epsilon_{max} = 10^{-2}$ . This embraces the solar value  $\epsilon \approx 5 \cdot 10^{-4}$  (Gizon 2002). Because at the maximum of solar activity,  $\delta \approx 10^\circ$ , we set  $\delta_{min} = 10^\circ$ . Note also that consistently with the discussion on Figure 2 of Section 3,  $\delta_{max} = 45^\circ$  is required.

Finally, the location parameter  $\theta_0$  has an uniform prior in the range  $[0, 90]^\circ$ .

The marginal likelihood of the model  $M_{AR}$  requires us to evaluate the triple integral,

$$P(\mathbf{O}|M) = \int \pi(\epsilon) \pi(\theta) \pi(\delta) L_2(\mathbf{O}|a_{2,m}, a_{4,m}, M) d\epsilon d\theta d\delta. \quad (\text{C.7})$$

The MCMC process used here involves the use of parallel Metropolis-Hastings tempered chains. The chains are mixing each other in order to enhance the sampling. As explained in Benomar et al. 2009, see their Section A.3, these parallel chains can be used to approximate the equation (C.7). This technique is here used with 10 parallel chains following a geometrical temperature law  $T_k = 1.7^{k-1}$ , with  $k$ , the chain index such that  $k = 1$  is the target distribution, given by equation (C.1).

## Appendix D: Bias map for $\widehat{HNR} = 10$ and $\widehat{HNR} = 20$

This section shows the bias on the  $a_1$ ,  $a_2$  and  $a_4$  coefficients in the case of  $\widehat{HNR} = 10$  or  $\widehat{HNR} = 20$ . The figure D.1 and D.3 are for the case of an equatorial band of activity and figure D.2 and D.4, for a polar cap. It is noticeable that the inaccuracy of the fit remains smaller than standard deviation in the majority of the parameter space and for  $i > 30^\circ$ ,  $a_1/\Gamma_{v_{max}} > 0.4$ . Interestingly, the relative-to-error bias on  $a_1$  is more pronounced in the case of an equatorial band of activity and for  $\{a_1/\Gamma_{v_{max}} \leq 0.4, i = [30, 60]\}$  (Figure D.1d and D.3d) and can exceed 3 times the uncertainty. The accuracy of the inference of activity based on the  $a$ -coefficients is expected to weakly depend on the  $\widehat{HNR}$  (although potentially with large uncertainty) for most stars, except within this regime (in addition to the gray area), where the centrifugal effect will be overestimated.

## Appendix E: Figures of the best fits

This section presents visuals on the best MCMC fits for the power spectrum of the active Sun (Figure E.1), quiet Sun (Figure E.2), 16 Cyg A (Figure E.3) and for the two  $a_4$  solutions of 16 Cyg B (Figures E.4 and E.5). For 16 Cyg B, the solutions are here separated by selecting the median for the samples only below or above  $a_4 = 21nHz$ . In the case of the Sun, the impact of the activity on the profile of  $l = 2$  is very clear, as the shifts of the m-components introduces an asymmetry in power for the overall  $l = 2$  mode profile during the active phase. During the quiet phase such an asymmetry is not visible.

Similarly and although it is less pronounced than in the Sun, in the case of 16 Cyg A and B, a weak asymmetry is visible on

$l = 2$  modes. For 16 Cyg B, the two solutions of  $a_4$  provide sensibly similar mode profiles as the difference is weakly apparent to the eye only for  $l = 2$ . The residuals do not show striking differences. This visually supports the fact that goodness of the fit is similar and explain that the two solutions co-exists in statistical terms.

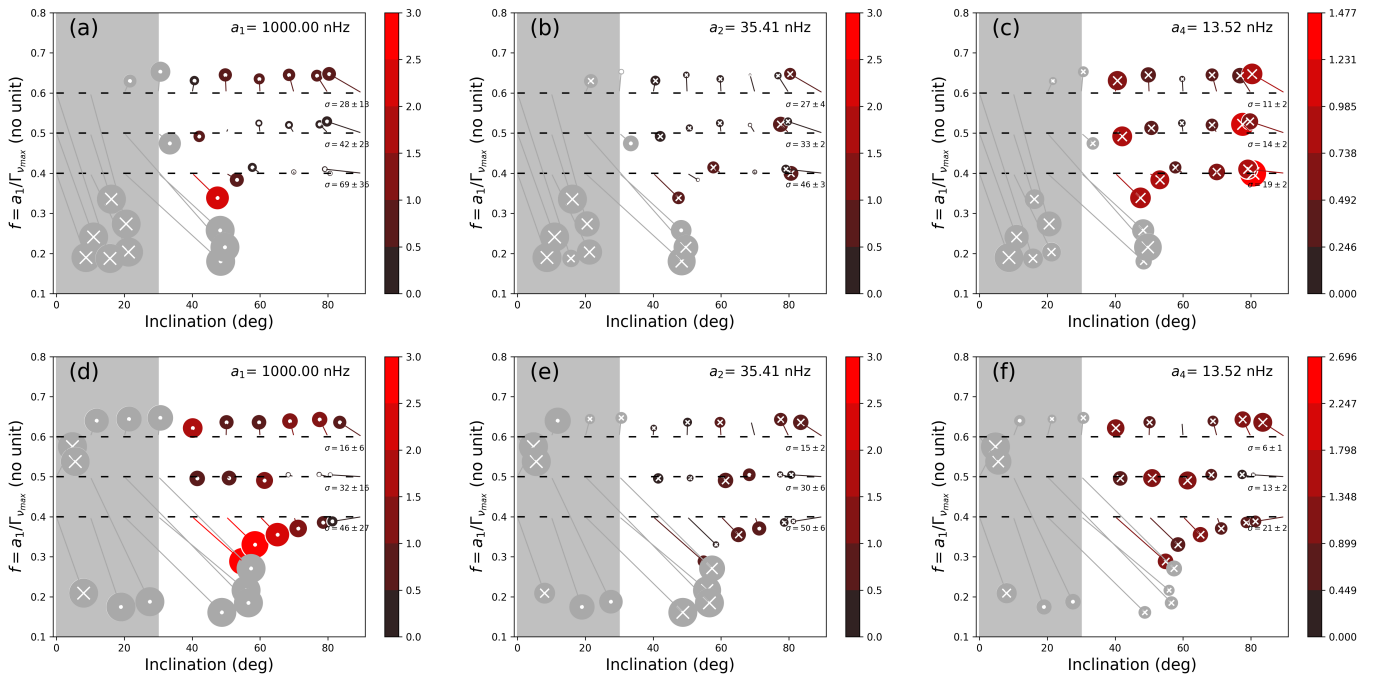


**Fig. D.1.** Bias analysis for  $HNR = 10$  for an equatorial activity band ( $\theta_0 = 85, \delta = 10$ ) of similar intensity to the Sun ( $\epsilon_{nl} = 5.10^{-4}$ ), for  $T_{obs} = 2$  years (top) and  $T_{obs} = 4$  years (bottom).

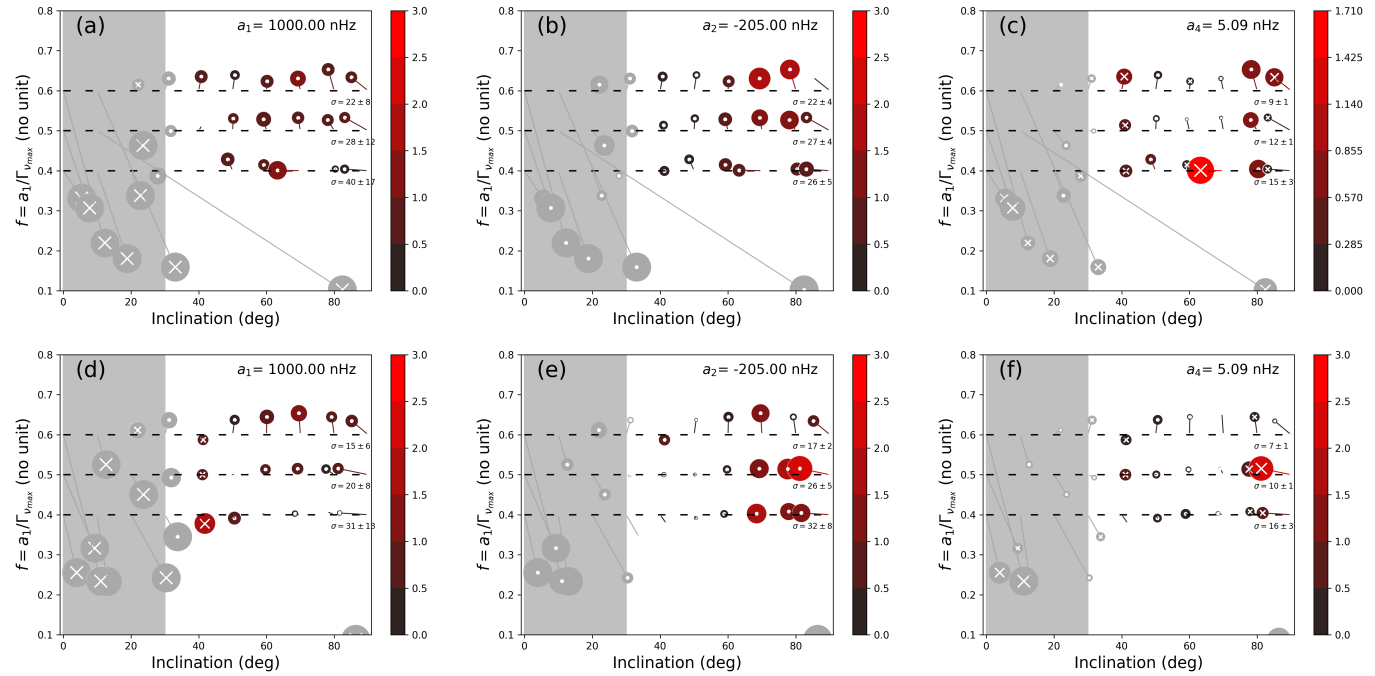


**Fig. D.2.** Bias analysis for  $HNR = 10$  for a large polar activity cap ( $\theta_0 = 22.5^\circ, \delta = 45^\circ$ ) of similar intensity to the Sun ( $\epsilon_{nl} = 5.10^{-4}$ ), for  $T_{obs} = 2$  years (top) and  $T_{obs} = 4$  years (bottom).

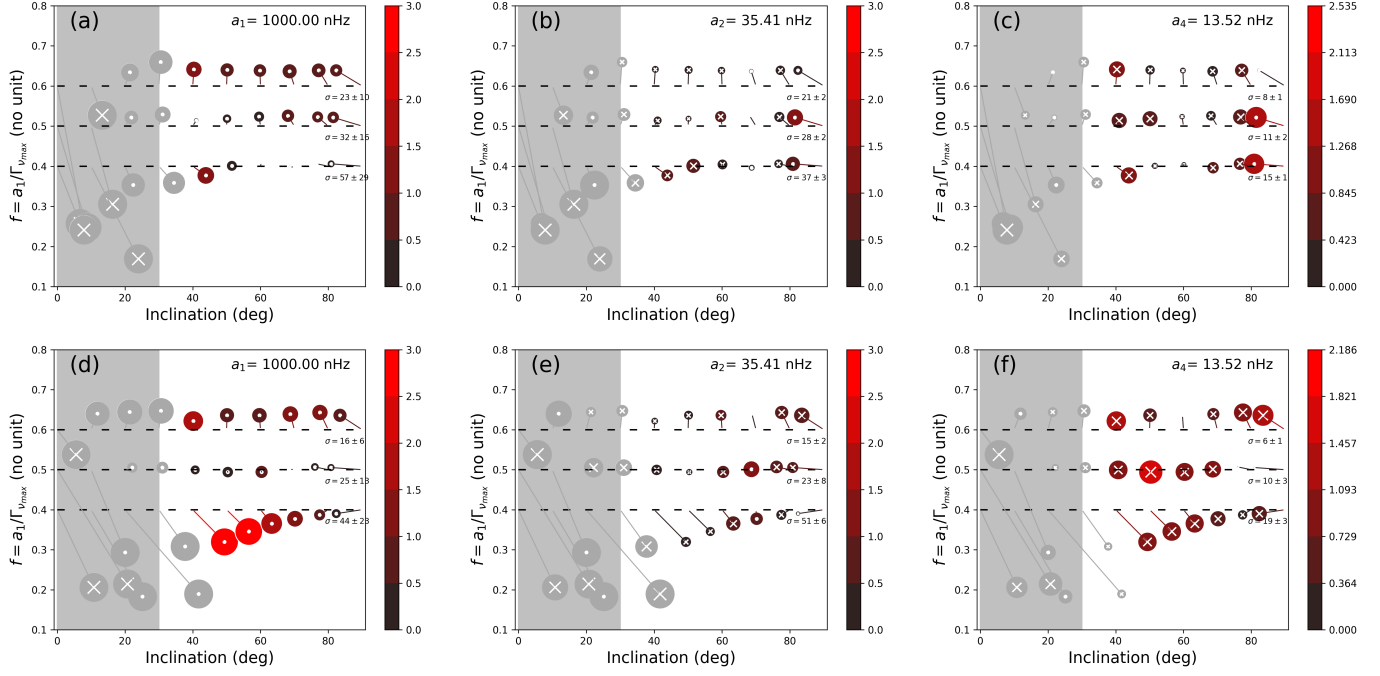


**Fig. D.3.** Bias analysis for  $\widehat{HNR} = 20$  for an equatorial activity band ( $\theta_0 = 85, \delta = 10$ ) of similar intensity to the Sun ( $\epsilon_{nl} = 5.10^{-4}$ ), for  $T_{obs} = 2$  years (top) and  $T_{obs} = 4$  years (bottom).

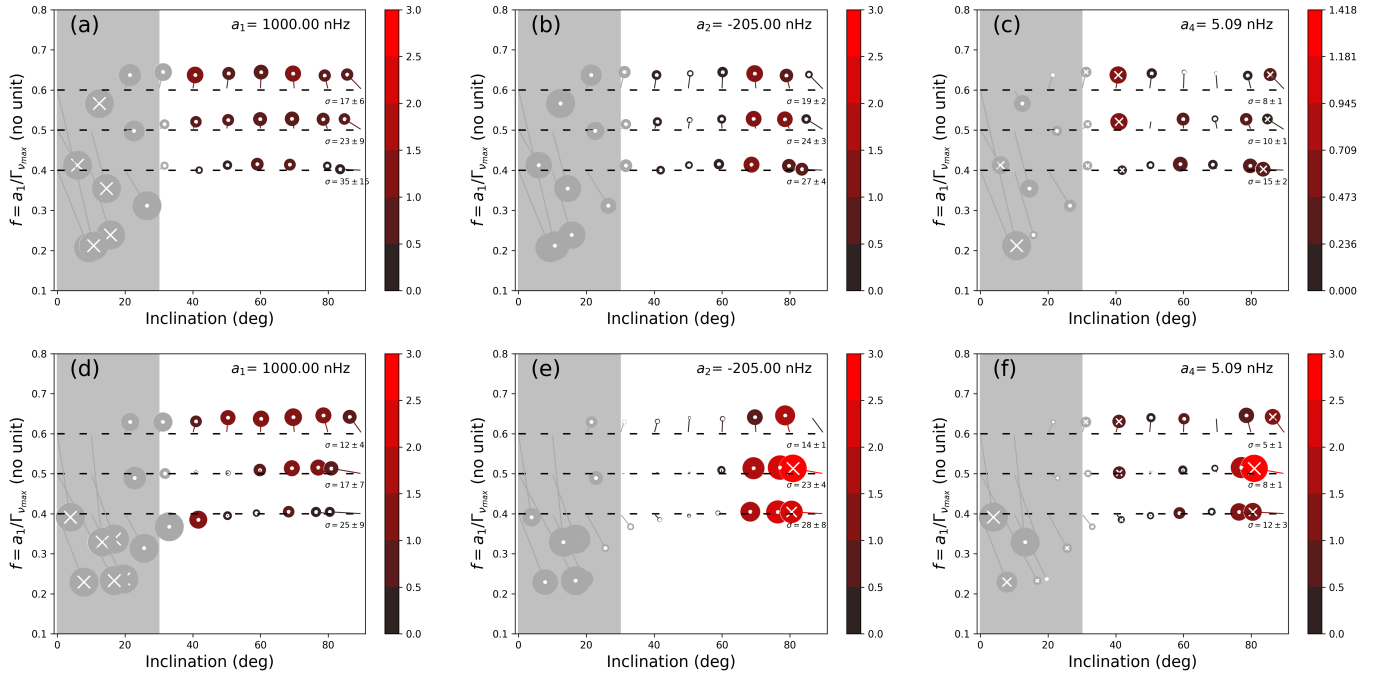


**Fig. D.4.** Bias analysis for  $\widehat{HNR} = 20$  for a large polar activity cap ( $\theta_0 = 22.5, \delta = 45$ ) of similar intensity to the Sun ( $\epsilon_{nl} = 5.10^{-4}$ ), for  $T_{obs} = 2$  years (top) and  $T_{obs} = 4$  years (bottom).

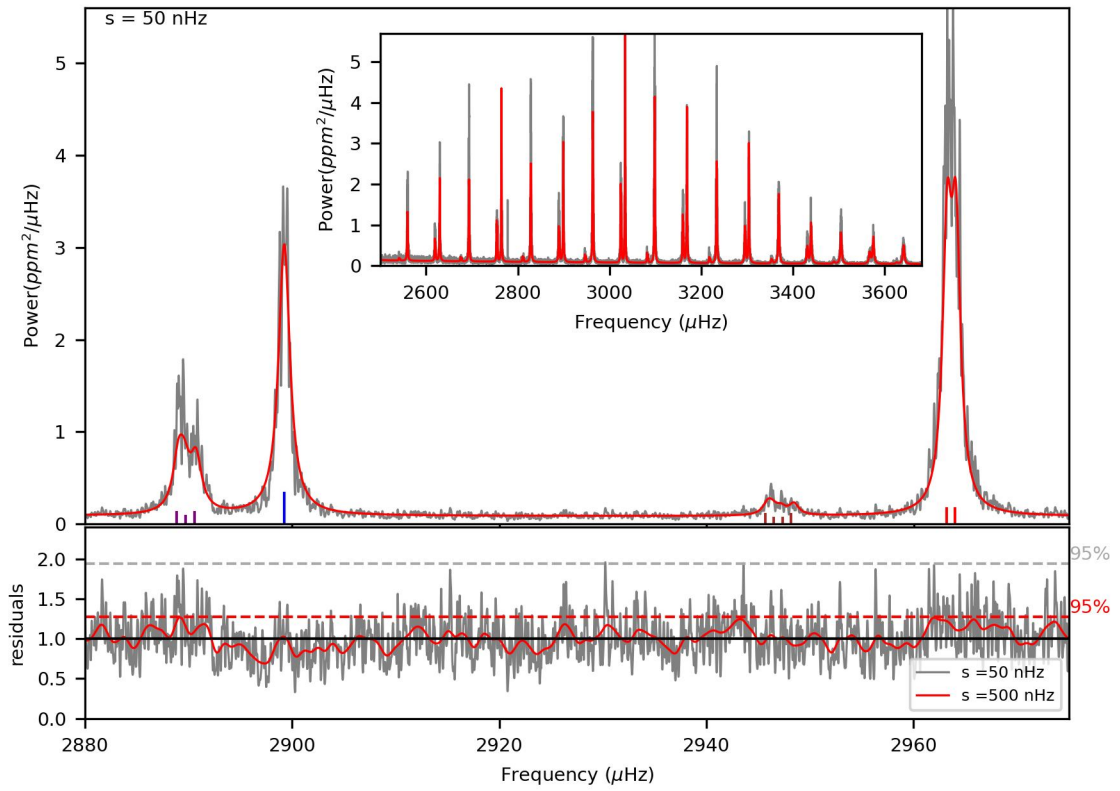


**Fig. E.1.** Solar power spectrum for observation between 1999 and 2002 after Gaussian smoothing over a kernel width  $s=50\text{ nHz}$ . Superimposed is the best MCMC fit. Top. Highlight of a  $l = 2, 0, 3, 1$  mode group (left to right) and their fit (red). The power asymmetry due to non-symmetric  $m$  components is visible in the data. Inset. Overall view of the modes. Bottom. Residual of the fit with two level  $s$  of Gaussian smoothing.

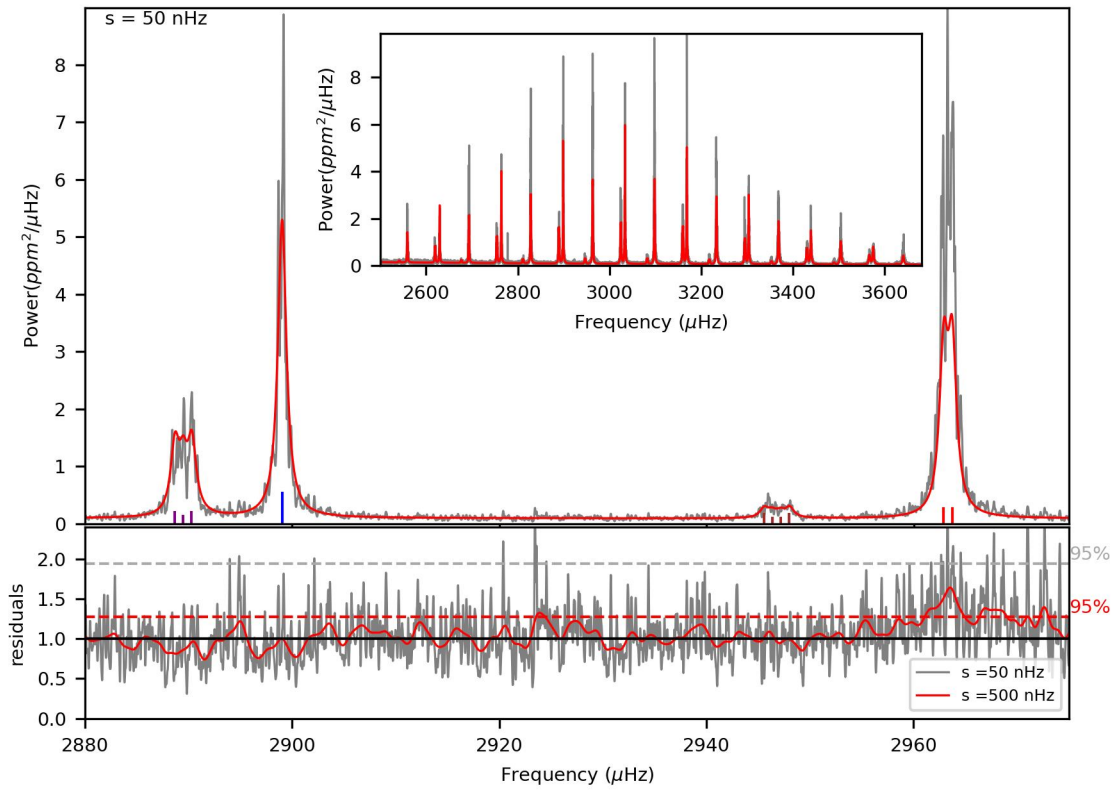


**Fig. E.2.** Same as Figure E.1 but between 2006 and 2009. Top. Highlight of a  $l = 2, 0, 3, 1$  mode group (left to right) and their fit (red). The power asymmetry seen for 1999-2002 is not apparent in the data. Inset. Overall view of the power spectrum. Bottom. Residual of the fit with two level s of Gaussian smoothing. The residual on  $l = 1$  is a bit high here due to the fix visibility for all modes.

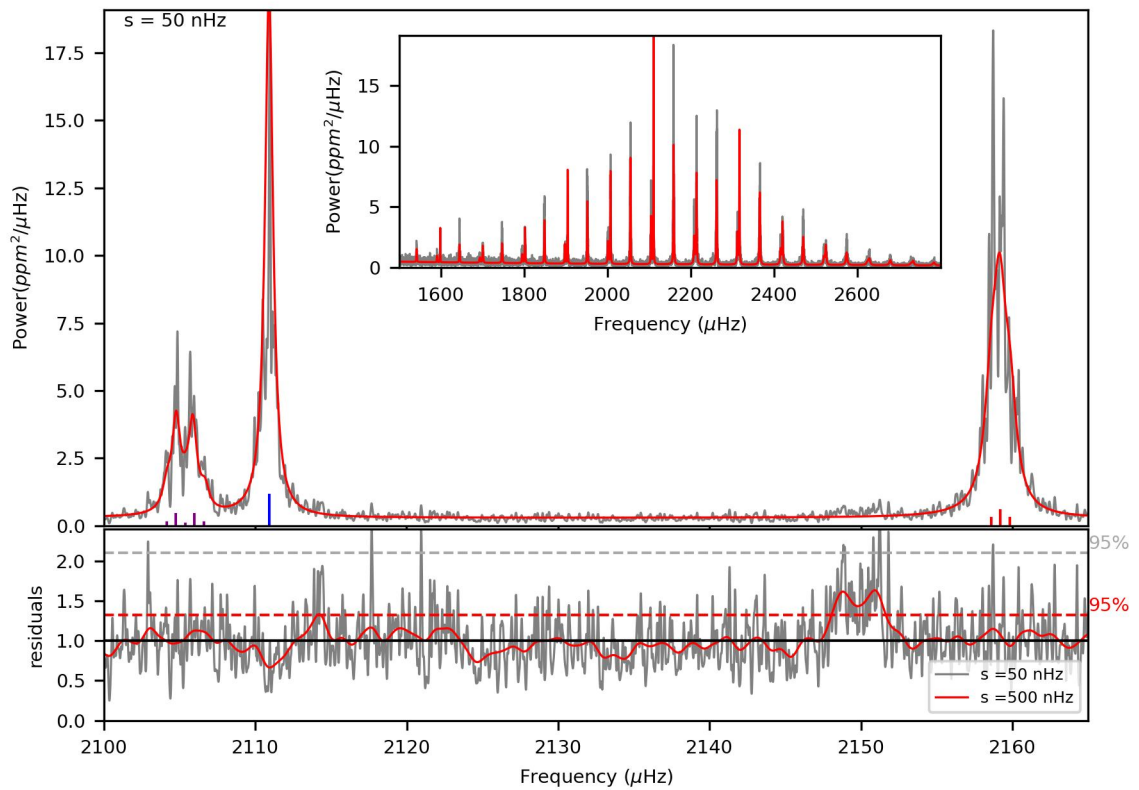


**Fig. E.3.** Same as Figure E.1 but for 16 Cyg A. Top. Highlight of a  $l = 2, 0, 1$  mode group (left to right) and their fit (red). A very mild power asymmetry is seen on the  $l = 2$  data. Inset. Overall view of the power spectrum. Bottom. Residual of the fit with two level  $s$  of Gaussian smoothing. The residual show an excess of power due to the low HNR  $\approx 1.7$   $l = 3$  (not fitted here).

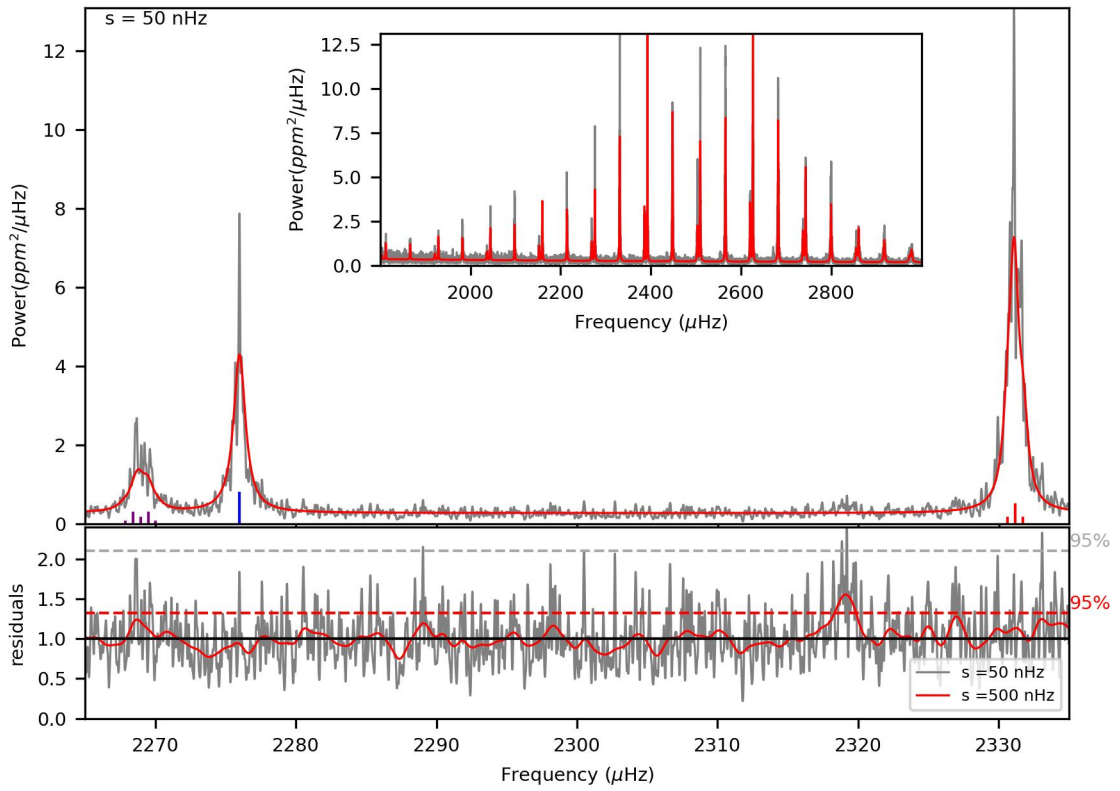


**Fig. E.4.** Same as Figure E.1 but for 16 Cyg B,  $a_4 < -21$  nHz. Top. Highlight of a  $l = 2, 0, 1$  mode group (left to right) and their fit (red). A mild power asymmetry is seen on the  $l = 2$  data. Inset. Overall view of the power spectrum. Bottom. Residual of the fit with two level  $s$  of Gaussian smoothing. The residual show an excess of power due to the low HNR  $\approx 1.6$   $l = 3$  (not fitted here).

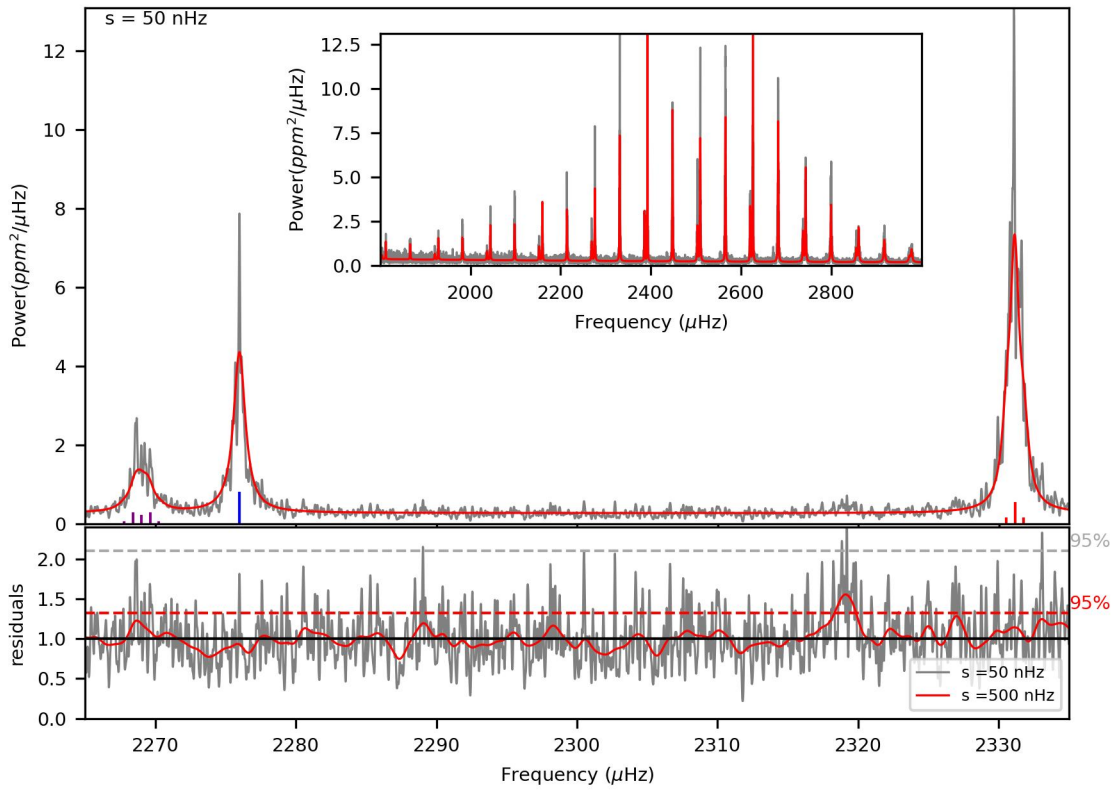


**Fig. E.5.** Same as Figure E.1 but for 16 Cyg B,  $a_4 > -21 \text{ nHz}$ . Top. Highlight of a  $l = 2, 0, 1$  mode group (left to right) and their fit (red). Inset. Overall view of the power spectrum. Bottom. Residual of the fit with two level  $s$  of Gaussian smoothing. The residual show an excess of power due to the low HNR  $\approx 1.6$  ( $l = 3$  not fitted here).

1278 **References**

- 1279 Anderson, E. R., Duvall, Jr., T. L., & Jefferies, S. M. 1990, *ApJ*, 364, 699
- 1280 Antia, H. M., Chitre, S. M., & Thompson, M. J. 2000, *A&A*, 360, 335
- 1281 Appourchaux, T. 2003, *A&A*, 412, 903
- 1282 Appourchaux, T., Antia, H. M., Benomar, O., et al. 2014, *A&A*, 566, A20
- 1283 Appourchaux, T., Gizon, L., & Rabello-Soares, M.-C. 1998, *A&AS*, 132, 107
- 1284 Appourchaux, T., Michel, E., Auvergne, M., et al. 2008, *A&A*, 488, 705
- 1285 Atchadé, Y. F. 2006, *Methodology and Computing in Applied Probability*, 8, 235
- 1286 Baglin, A., Auvergne, M., Barge, P., et al. 2006, in *ESA Special Publication*, Vol. 1306, *ESA Special Publication*, ed. M. Fridlund, A. Baglin, J. Lochard, & L. Conroy, 33
- Ballot, J., Barban, C., & van't Veer-Mennenet, C. 2011, *A&A*, 531, A124
- Bazot, M. 2020, *A&A*, 635, A26
- Bazot, M., Benomar, O., Christensen-Dalsgaard, J., et al. 2019, *A&A*, 623, A125
- Bellinger, E. P., Basu, S., Hekker, S., & Ball, W. H. 2017, *ApJ*, 851, 80
- Benomar, O. 2008, *Communications in Asteroseismology*, 157, 98
- Benomar, O., Appourchaux, T., & Baudin, F. 2009, *A&A*, 506, 15
- Benomar, O., Bazot, M., Nielsen, M. B., et al. 2018a, *Science*, 361, 1231
- Benomar, O., Bedding, T. R., Stello, D., et al. 2012, *ApJ*, 745, L33
- Benomar, O., Goupil, M., Belkacem, K., et al. 2018b, *ApJ*, 857, 119
- Benomar, O., Takata, M., Shibahashi, H., Ceillier, T., & García, R. A. 2015, *MNRAS*, 452, 2654
- Bishop, C. M. 1995, *Neural Networks for Pattern Recognition* (Oxford University Press, Inc)
- Borucki, W. J., Koch, D., Basri, G., et al. 2010, *Science*, 327, 977
- Brun, A. S. & Browning, M. K. 2017, *Living Reviews in Solar Physics*, 14, 4
- Buldgen, G., Farnir, M., Eggenberger, P., et al. 2022, *A&A*, 661, A143
- Buldgen, G., Reese, D. R., & Dupret, M. A. 2015, *A&A*, 583, A62
- Campante, T. L., Handberg, R., Mathur, S., et al. 2011, *A&A*, 534, A6
- Campante, T. L., Lund, M. N., Kuszelwicz, J. S., et al. 2016, *ApJ*, 819, 85
- Catura, R. C., Acton, L. W., & Johnson, H. M. 1975, *ApJ*, 196, L47
- Ceillier, T., Tayar, J., Mathur, S., et al. 2017, *A&A*, 605, A111
- Chandrasekhar, S. 1969, *Ellipsoidal figures of equilibrium*
- Chaplin, W. J., Elsworth, Y., Isaak, G. R., et al. 2003, *Monthly Notices of the Royal Astronomical Society*, 343, 343
- Cochran, W. D., Hatzes, A. P., Butler, R. P., & Marcy, G. W. 1997, *ApJ*, 483, 457
- Davies, G. R., Chaplin, W. J., Farr, W. M., et al. 2015, *MNRAS*, 446, 2959
- Deal, M., Richard, O., & Vauclair, S. 2015, *A&A*, 584, A105
- Deheuvels, S., Doğan, G., Goupil, M. J., et al. 2014, *A&A*, 564, A27
- Deheuvels, S., García, R. A., Chaplin, W. J., et al. 2012, *ApJ*, 756, 19
- Deliyannis, C. P., Cunha, K., King, J. R., & Boesgaard, A. M. 2000, *AJ*, 119, 2437
- Duvall, Jr., T. L., Jefferies, S. M., Harvey, J. W., Osaki, Y., & Pomerantz, M. A. 1993, *ApJ*, 410, 829
- Dziembowski, W. A., Goode, P. R., Kosovichev, A. G., & Schou, J. 2000, *ApJ*, 537, 1026
- Farnir, M., Dupret, M. A., Buldgen, G., et al. 2020, *A&A*, 644, A37
- Frohlich, C., Andersen, B. N., Appourchaux, T., et al. 1997, *Sol. Phys.*, 170, 1
- García, R. A., Hekker, S., Stello, D., et al. 2011a, *MNRAS*, 414, L6
- García, R. A., Salabert, D., Ballot, J., et al. 2011b, *Journal of Physics Conference Series*, 271, 012049
- Gehan, C., Mosser, B., Michel, E., Samadi, R., & Kallinger, T. 2018, *A&A*, 616, A24
- Georgobiani, D., Kosovichev, A. G., Nigam, R., Nordlund, Å., & Stein, R. F. 2000, *ApJ*, 530, L139
- Gizon, L. 2002, *Astronomische Nachrichten*, 323, 251
- Gizon, L. 2006, *Central European Astrophysical Bulletin*, 30, 1
- Gizon, L., Ballot, J., Michel, E., et al. 2013, *Proceedings of the National Academy of Science*, 110, 13267
- Gizon, L., Sekii, T., Takata, M., et al. 2016, *Science Advances*, 2, e1601777
- Gizon, L. & Solanki, S. K. 2003, *ApJ*, 589, 1009
- Gizon, L. & Solanki, S. K. 2004, *Sol. Phys.*, 220, 169
- Gough, D. O. & Taylor, P. P. 1984, *Mem. Soc. Astron. Italiana*, 55, 215
- Gough, D. O. & Thompson, M. J. 1990, *MNRAS*, 242, 25
- Gregory, P. C. 2005, *Bayesian Logical Data Analysis for the Physical Sciences: A Comparative Approach with 'Mathematica' Support*
- Handberg, R. & Campante, T. L. 2011, *A&A*, 527, A56
- Hansen, C. J., Cox, J. P., & van Horn, H. M. 1977, *ApJ*, 217, 151
- Hartmann, L. & Rosner, R. 1979, *ApJ*, 230, 802
- Harvey, J. 1985, *ESA SP*, 235, 199
- Hogg, D. W., Myers, A. D., & Bovy, J. 2010, *ApJ*, 725, 2166
- Huber, D., Bedding, T. R., Stello, D., et al. 2011, *ApJ*, 743, 143
- Jeffreys, H. 1961, *Theory of Probability*, 3rd edn. (Oxford, England: Oxford)
- Kamiaka, S., Benomar, O., & Suto, Y. 2018, *MNRAS*, 479, 391
- King, J. R., Deliyannis, C. P., Hiltgen, D. D., et al. 1997, *AJ*, 113, 1871
- Libbrecht, K. G. & Woodard, M. F. 1990, *Nature*, 345, 779
- Lignières, F., Rieutord, M., & Reese, D. 2006, *A&A*, 455, 607
- Lund, M. N., Lundkvist, M., Silva Aguirre, V., et al. 2014, *A&A*, 570, A54
- Lund, M. N., Silva Aguirre, V., Davies, G. R., et al. 2017, *ApJ*, 835, 172
- Maeder, A. & Meynet, G. 2008, in *Astronomical Society of the Pacific Conference Series*, Vol. 388, *Mass Loss from Stars and the Evolution of Stellar Clusters*, ed. A. de Koter, L. J. Smith, & L. B. F. M. Waters, 3
- Maia, M. T., Meléndez, J., Lorenzo-Oliveira, D., Spina, L., & Jofré, P. 2019, *A&A*, 628, A126
- Mathur, S., García, R. A., Régulo, C., et al. 2010, *A&A*, 511, A46
- Metcalfe, T. S., Chaplin, W. J., Appourchaux, T., et al. 2012, *ApJ*, 748, L10
- Metcalfe, T. S., Egeland, R., & van Saders, J. 2016, *ApJ*, 826, L2
- Morel, T., Creevey, O. L., Montalbán, J., Miglio, A., & Willett, E. 2021, *A&A*, 646, A78
- Mosser, B., Goupil, M. J., Belkacem, K., et al. 2012, *A&A*, 540, A143
- Neckel, H. 1986, *A&A*, 159, 175

- 1369 Nielsen, M. B., Schunker, H., Gizon, L., Schou, J., & Ball, W. H. 2017, A&A,  
 1370 603, A6  
 1371 Nigam, R. & Kosovichev, A. G. 1998, ApJ, 505, L51  
 1372 Nsamba, B., Cunha, M. S., Rocha, C. I. S. A., et al. 2022, MN-  
 1373 RAS[arXiv:2205.04972]  
 1374 Oláh, K., Kővári, Z., Petrovay, K., et al. 2016, A&A, 590, A133  
 1375 Oláh, K., Kolláth, Z., Granzer, T., et al. 2009, A&A, 501, 703  
 1376 Ouazzani, R. M., Marques, J. P., Goupil, M. J., et al. 2019, A&A, 626, A121  
 1377 Papini, E. & Gizon, L. 2019, Frontiers in Astronomy and Space Sciences, 6  
 1378 Pijpers, F. P. 1997, A&A, 326, 1235  
 1379 Pijpers, F. P. 1998, Ap&SS, 261, 17  
 1380 Ramírez, I., Meléndez, J., & Asplund, M. 2009, A&A, 508, L17  
 1381 Rauer, H., Catala, C., Aerts, C., et al. 2014, Experimental Astronomy, 38, 249  
 1382 Ricker, G. R., Winn, J. N., Vanderspek, R., et al. 2014, in Society of Photo-  
 1383 Optical Instrumentation Engineers (SPIE) Conference Series, Vol. 9143,  
 1384 Proc. SPIE, 914320  
 1385 Ritzwoller, M. H. & Lavelle, E. M. 1991, ApJ, 369, 557  
 1386 Roxburgh, I. W. 2017, A&A, 604, A42  
 1387 Schou, J., Christensen-Dalsgaard, J., & Thompson, M. J. 1994, ApJ, 433, 389  
 1388 Schuler, S. C., Cunha, K., Smith, V. V., et al. 2011, ApJ, 737, L32  
 1389 Silva-Valio, A., Lanza, A. F., Alonso, R., & Barge, P. 2010, A&A, 510, A25  
 1390 Simon, T., Ayres, T. R., Redfield, S., & Linsky, J. L. 2002, ApJ, 579, 800  
 1391 Stahn, T. 2010, PhD thesis, Georg August University of Gottingen, Germany  
 1392 Takeda, Y. 2005, PASJ, 57, 83  
 1393 Thompson, M. J., Christensen-Dalsgaard, J., Miesch, M. S., & Toomre, J. 2003,  
 1394 ARA&A, 41, 599  
 1395 Toutain, T., Appourchaux, T., Frohlich, C., et al. 1998, in ESA Special Publica-  
 1396 tion, Vol. 418, Structure and Dynamics of the Interior of the Sun and Sun-like  
 1397 Stars, ed. S. Korzennik, 973  
 1398 Toutain, T. & Gouttebroze, P. 1993, A&A, 268, 309  
 1399 Toutain, T. & Kosovichev, A. G. 2001, in ESA Special Publication, Vol. 464,  
 1400 SOHO 10/GONG 2000 Workshop: Helio- and Asteroseismology at the Dawn  
 1401 of the Millennium, ed. A. Wilson & P. L. Pallé, 123–126  
 1402 Ulrich, R. K. 1986, ApJ, 306, L37  
 1403 Unno, W., Osaki, Y., Ando, H., Saio, H., & Shibahashi, H. 1989, Nonradial Os-  
 1404 cillations of Stars (University Tokyo Press)  
 1405 van Saders, J. L., Ceillier, T., Metcalfe, T. S., et al. 2016, Nature, 529, 181  
 1406 Vaughan, A. H. 1983, in Solar and Stellar Magnetic Fields: Origins and Coronal  
 1407 Effects, ed. J. O. Stenflo, Vol. 102, 113–131  
 1408 Verma, K., Faria, J. P., Antia, H. M., et al. 2014, ApJ, 790, 138  
 1409 Walker, G., Matthews, J., Kuschnig, R., et al. 2003, PASP, 115, 1023  
 1410 White, S. M. 1999, Sol. Phys., 190, 309  
 1411 White, S. M., Iwai, K., Phillips, N. M., et al. 2017, Sol. Phys., 292, 88  
 1412 White, T. R., Bedding, T. R., Stello, D., et al. 2011, ApJ, 743, 161  
 1413 White, T. R., Huber, D., Maestro, V., et al. 2013, MNRAS, 433, 1262